Review—Investigation and Review of the Thermal, Mechanical, Electrical, Optical, and Structural Properties of Atomic Layer Deposited High-*k* Dielectrics: Beryllium Oxide, Aluminum Oxide, Hafnium Oxide, and Aluminum Nitride

John T. Gaskins,[a] Patrick E. Hopkins,[a,b,c,z] Devin R. Merrill,[d,e] Sage R. Bauers,[d] Erik Hadland,[d] David C. Johnson,[d,z] Donghyi Koh,[e,f] Jung Hwan Yum,[f] Sanjay Banerjee,[f,*] Bradley J. Nordell,[g] Michelle M. Paquette,[g] Anthony N. Caruso,[g] William A. Lanford,[h] Patrick Henry,[e] Liza Ross,[e] Han Li,[e] Liyi Li,[e] Marc French,[e] Antonio M. Rudolph,[e] and Sean W. King[e,*,z]

[a]*Department of Mechanical and Aerospace Engineering, University of Virginia, Charlottesville, Virginia 22904, USA*
[b]*Department of Materials Science and Engineering, University of Virginia, Charlottesville, Virginia 22904, USA*
[c]*Department of Physics, University of Virginia, Charlottesville, Virginia 22904, USA*
[d]*Department of Chemistry, University of Oregon, Eugene, Oregon 97403, USA*
[e]*Logic Technology Development, Intel Corporation, Hillsboro, Oregon 97124, USA*
[f]*Department of Electrical and Computer Engineering, Microelectronics Research Center, University of Texas at Austin, Austin, Texas 78758, USA*
[g]*Department of Physics and Astronomy, University of Missouri-Kansas City, Kansas City, Missouri 64110, USA*
[h]*Department of Physics, University at Albany, Albany, New York 12222, USA*

Atomic layer deposited (ALD) high-dielectric-constant (high-*k*) materials have found extensive applications in a variety of electronic, optical, optoelectronic, and photovoltaic devices. While electrical, optical, and interfacial properties have been the primary consideration for such devices, thermal and mechanical properties are becoming an additional key consideration for many new and emerging applications of ALD high-*k* materials in electromechanical, energy storage, and organic light emitting diode devices. Unfortunately, a clear correspondence between thermal/mechanical and electrical/optical properties in ALD high-*k* materials has yet to be established, and a detailed comparison to conventional silicon-based dielectrics to facilitate optimal material selection is also lacking. In this regard, we have conducted a comprehensive investigation and review of the thermal, mechanical, electrical, optical, and structural properties for a series of prevalent and emerging ALD high-*k* materials including aluminum oxide (Al_2O_3), aluminum nitride (AlN), hafnium oxide (HfO_2), and beryllium oxide (BeO). For comparison, more established silicon-based dielectrics were also examined, including thermally grown silicon dioxide (SiO_2) and plasma-enhanced chemically vapor deposited hydrogenated silicon nitride (SiN:H). We find that in addition to exhibiting high values of dielectric permittivity and electrical resistance that exceed those of SiO_2 and SiN:H, the ALD high-*k* materials exhibit equally exceptional thermal and mechanical properties with coefficients of thermal expansion $\leq 6 \times 10^{-6}$ /°C, thermal conductivites (κ) of 3–15 W/m K, and Young's modulus and hardness values exceeding 200 and 25 GPa, respectively. In many cases, the observed extreme thermal/mechanical properties correlate with the presence of crystallinity in the ALD high-*k* films. In contrast, some of the electrical and optical properties correlate more strongly with the percentage of ionic vs. covalent bonds present in the high-*k* film. Overall, the ALD high-*k* dielectrics investigated concurrently exhibit compelling thermal/mechanical and electrical/optical properties.

The drive to reduce gate leakage currents in highly scaled complementary metal–oxide–semiconductor (CMOS) transistors has led to the exploration and development of a wide variety of high-dielectric-constant (high-*k*) materials to replace silicon dioxide (SiO_2) as the insulating gate dielectric material.[1–8] Many of these same high-*k* materials have found additional applications in future non-CMOS logic and memory storage products such as solid-state electrolytes in resistive switching devices,[9,10] tunnel barriers in spin-transport devices,[11] and as a ferroelectric in magnetoelectric devices.[12,13] They have also enabled significant performance gains in a wide variety of energy storage,[14,15] photovoltaic,[16,17] optoelectronic,[18] high-frequency,[19,20] high-power,[21] and high-temperature devices.[22] Due to exceptional thickness control and uniformity, atomic layer deposition (ALD) has become the preferred method for depositing most high-*k* dielectric materials in micro-/nano-electronic applications.[23] The low deposition temperature,[23] excellent surface topography coverage,[23–25] low pinhole/defect density,[26,27] high mass/atomic density,[28] and thermodynamic stability[29] of ALD high-*k* materials have further enabled these materials to serve additional roles in complex interference coatings[30] as well as in moisture,[31] oxygen,[32] and metal[33] diffusion barriers in hermetic packaging,[34] organic light emitting diode,[35] and metal interconnect[36] applications.

While electrical, physical, and thermodynamic properties have clearly been a key consideration in all of the above applications, thermal properties have become an additional important consideration for higk-*k* dielectrics as aggressive dimensional scaling of devices has created the need to dissipate significant amounts of heat at the macroscale[37,38] and self-induced device heating effects have become significant reliability concerns at the nanoscale.[39–41] The mechanical properties of high-*k* dielectrics have also become a key consideration for the implementation of these materials in various nanoelectromechanical (NEM)[42,43] and flexible micro-/nano-electronic devices.[44,45] For such devices, knowledge of properties such as Young's modulus and film stress are critical for predicting the flexure and resonance frequencies of bridged and cantilevered switches and sensors,[46–49] stretched transistor device performance,[50,51] buckling failures in nanopatterned structures,[52,53] and macroscale buckling and nanoscale wrinkling effects for stiff high-*k* films deposited on compliant polymeric substrates.[54,55]

Unfortunately, only a limited number of studies have reported on the thermal[56–59] and mechanical[42,60–66] properties of ALD high-*k* dielectric materials, and the numerous reviews[2–8] of high-*k* dielectrics have focused primarily on the electronic structure and interfacial properties of high-*k* dielectrics from a CMOS device perspective. To the authors' knowledge, a clear correspondence between thermal/mechanical and electrical/optical properties for ALD high-*k* dielectrics has yet to be established. In this regard, we have conducted

a detailed investigation and review of the thermal and mechanical properties for a series of state-of-the-art and emerging ALD high-k dielectric materials combined with complementary chemical composition, atomic/nano-structure, electrical, and optical property characterization of these same materials. The combined characterization allows for a complete perspective on the full spectrum of material properties and structure–property–processing relationships exhibited by ALD high-k materials.

The high-k materials chosen for this investigation were those most commonly utilized in the CMOS industry and/or emerging for consideration in future logic, memory, energy storage, NEM and other device applications, and specifically include aluminum oxide (Al_2O_3), aluminum nitride (AlN), hafnium oxide (HfO_2), and beryllium oxide (BeO). Al_2O_3 was one of the earliest candidates considered to replace SiO_2 as the CMOS gate dielectric, but has since been supplanted by HfO_2 primarily due to its higher dielectric constant (Al_2O_3 $k = 8$–10 vs. HfO_2 $k \sim 25$).[2] However, due to large band gaps[2–4] and favorable valence and conduction band alignments,[4,67–69] Al_2O_3 and HfO_2 both continue to play an important role as high-k dielectrics in three-dimensional (3D) memory and energy storage structures,[14,20] RF blocking/decoupling capacitors,[15,20] high-mobility and tunnel field effect III–V devices,[70–72] high-power, high-frequency, and high-temperature III–N devices,[21,22,73,74] and 2D transition metal dichalcogenide CMOS devices.[75–77] In addition, the high thermodynamic stability[29] and atomic/mass density[28] of Al_2O_3 has enabled it to serve as an optical coating material,[30] surface passivation layer in Si solar cells,[16,78] hermetic encapsulation layer for OLED and packaging applications,[34,35] metal[36] and gas[27,31,32] diffusion barrier in microelectronic applications, and as a corrosion and stiction protection layer in NEM devices.[79] The high mechanical properties[42] of Al_2O_3 have further enabled its use as a wear-resistant coating in NEM devices,[79] bridge or cantilever in nanomechanical resonator devices,[80] or post-fabrication frequency tuning layer for resonant devices.[49,81]

AlN was similarly an early high-k candidate to replace SiO_2 in CMOS device applications as both a gate dielectric[82,83] and reaction barrier layer for other oxide high-k dielectrics.[84] It has also been examined as a gate dielectric in III–V devices where particularly close lattice matching exists with GaN.[85,86] The piezoelectric properties of AlN[87] have additionally made it of interest as a transducer material in surface acoustic wave and NEM devices.[43,88] The high resistance of AlN to fluorinated plasmas[89] has further lead to its use as a plasma etch stop,[33] hard mask,[90,91] and Cu capping layer[33] in microelectronic device applications.

As with Al_2O_3 and AlN, the many compelling properties of HfO_2 have likewise led to its use in a variety of other non-traditional high-k applications. In particular, the high refractive index,[2] atomic/mass density,[18] and mechanical properties[92,93] of HfO_2 have made it a favorable choice as a protective and wear-resistant film in complex optical interference and reflective coatings,[30,94,95] and as a pore sealant,[96] selectively grown hard-mask,[97] and Cu diffusion barrier[36] in low-dielectric-constant (low-k) metal interconnects. The unique defect and surface chemistry of HfO_2 has further led to its use as a solid-state electrolyte in valence change resistive switching devices,[9,10] catalytic surface material in gas sensors,[98] and even garnered some interest as an antibacterial coating in bioNEMS applications.[99] Lastly, the recently discovered ferroelectric properties[100,101] of HfO_2 have also led to renewed interest in ferroelectric based memory[102] and the development of new negative capacitance devices.[103]

BeO, in contrast to Al_2O_3, AlN, and HfO_2, is a new emerging high-k dielectric. Owing to an exceptionally high thermal conductivity, bulk BeO has already been utilized as a thermal heat sink substrate in demanding heat dissipation, microwave, and high-power applications.[104] More recently, BeO has shown great promise as a barrier layer and gate dielectric in both Si CMOS and III–V high-power and high-frequency device applications,[105–109] and as an alloying agent and oxygen diffusion barrier for ZnO-based optoelectronic devices.[110–112] As we will show, ALD BeO exhibits several compelling properties which may make it useful in many additional high-performance applications where extremes in material properties are required.

For comparison, conventional silicon-based dielectrics were also investigated, including thermally-grown silicon dioxide (SiO_2) and plasma-enhanced chemically vapor deposited (PECVD) amorphous hydrogentated silicon nitride (SiN:H). Thermally grown SiO_2 represents the traditional CMOS gate oxide dielectric material[2] and is also representative of the plasma deposited SiO_2 intermetal and interlayer dielectric (ILD) materials historically utilized in back-end-of-line metal interconnects.[113,114] PECVD SiN:H similarly represents the commonly utilized gate dielectric in a-Si:H thin-film transistor (TFT) technologies,[115,116] and has also been considered as a gate dielectric for organic TFTs[116] and as an anti-reflection coating[117] and surface passivation layer in Si solar cell technologies.[118] In CMOS logic, memory, NEM and other microelectronic device applications, a-SiN:H is instead more commonly utilized either as a dielectric diffusion barrier, etch stop, or hermetic encapsulation layer.[119,120]

To compare and contrast the above materials, their full spectrum of thermal, mechanical, electrical, optical, and chemical properties was measured. The thermal properties investigated include thermal conductivity (κ) and interfacial thermal resistance, as measured by time domain thermoreflectance (TDTR), and coefficient of thermal expansion (CTE) as determined by heated wafer curvature and X-ray reflectivity (XRR) thickness measurements. The mechanical properties investigated include Young's modulus (Y) and hardness (H), as determined by nanoindentation measurements, and intrinsic film stress as determined by wafer curvature changes and Stoney's formula. The combined thermal/mechanical characterization is further supported by additional electrical, optical, elemental composition, bond structure, and crystal structure characterization performed using techniques such as current–voltage (IV) and capacitance–voltage (CV) probing, spectroscopic ellipsometry, combined nuclear reaction analysis and Rutherford backscattering (NRA-RBS), Fourier-transform infrared (FTIR) spectroscopy, X-ray diffraction (XRD), and atomic force microscopy (AFM). The combined results show that all the investigated high-k materials exhibit robust thermal/mechanical properties while retaining equivalent electrical/optical properties relative to more established silicon-based dielectrics such as SiO_2 and SiN:H. In some cases, the high thermal/mechanical properties also correlate with the observation of some degree of crystallinity in the as-deposited films.

Experimental

High-k film deposition.—Nominally 200 nm thick Al_2O_3, AlN, and HfO_2 films were grown on double-side polished, 300 mm diameter silicon (001) substrates via thermal ALD and plasma-enhanced ALD (PEALD) at temperatures on the order of 350°C using industry-standard precursors and commercially available ALD tools.[33,121] The Al_2O_3 and HfO_2 films were grown by ALD using alternating pulses of trimethylaluminum (TMA) and water (H_2O) and hafnium tetrachloride ($HfCl_4$) and H_2O, respectively. The AlN films were grown by PEALD using alternating doses of TMA and a nitrodizing NH_3 plasma.[33] A nominally 100 nm thick BeO film was grown on coupons cut from 200 mm diameter Si (001) substrates via thermal ALD using alternating exposures of diethylberyllium (DEB) and H_2O at 250°C.[122–124] Due to the significantly lower deposition temperature, the ALD BeO film was given an additional rapid thermal anneal to 600°C. The Al_2O_3, AlN, and HfO_2 films did not receive any post deposition anneals. For comparison, SiO_2 and SiN:H films were grown on 300 mm diameter silicon (001) substrates via thermal oxidation and PECVD, respectively.[125,126]

We do note that the above mentioned film thicknesses are significantly higher than those typically utilized in traditional Si CMOS high-k dielectric applications where thicknesses of <10 nm are more common.[2–8] However, many of the applications involving these materials as diffusion barriers,[27,31,127] nano-resonators,[80,81] and piezoelectric transducers[43,87] can require significantly higher thicknesses of 20–1000 nm. Also, use of film thicknesses >100 nm minimize substrate[128] and interfacial thermal boundary resistance[129] effects that can complicate the mechanical and thermal property measurements, respectively. As the film thickness requirements for applications

demanding thermal and mechanical properties align with their corresponding metrologies and do not inherently impact the electrical, optical, and chemical analysis, we have chosen to use film thicknesses in the 100–200 nm range throughout this study.

Elemental composition and micro-/nano-structure analysis.—
The elemental composition for the high-*k* films was determined by combined nuclear reaction analysis and Rutherford backscattering (NRA-RBS) measurements performed at the Albany Dynamitron Accelerator Laboratory. This analysis has been described in detail previously.[130] Briefly, the H analysis was performed using the ^{15}N nuclear reaction method. This method makes use of a resonant nuclear reaction between ^{15}N and H in the target material. By measuring the number of characteristic gamma-rays from this reaction versus beam energy, the H concentration versus depth in the target was determined. The Be, C, N, and O contents were determined using deuteron nuclear reactions. The samples were bombarded with a deuteron beam at 1.2 MeV and the ^{9}Be(d,p$_0$), ^{12}C(d,p$_o$), ^{14}N(d,α_1), and ^{16}O(d,p$_o$) nuclear reactions were used to determine the Be, C, N, and O contents of the film (in atoms/cm^2).[130] Rutherford backscattering spectrometry (RBS) utilizing 2 MeV ^{4}He was used to determine the Al and Hf contents. With the film's absolute H, Be, C, N, O, Al, and Hf composition known, parameter-free simulations of the full RBS spectra were performed using the program RUMP.[130] These RUMP simulations were then compared to the measured full RBS spectrum providing a powerful check of the analysis. As a consistency check, the mass density for all of the high-*k* films was determined using both NRA-RBS and previously described XRR measurements.[131] The two techniques were found to be in agreement to within ± 0.1 g/cm^3.

The chemical bonding and local chemical structure for the high-*k* films was investigated using Fourier transform infrared (FTIR) spectroscopy. Transmission FTIR spectra of the Al$_2$O$_3$, AlN, and HfO$_2$ films were collected at room temperature using a Nicolet Magna-IR 860 spectrometer.[131,132] All spectra were collected in transmission mode, and the Si substrate background was subtracted by pre-scanning a bare Si wafer and subtracting the resulting spectrum from that of the high-*k*/Si sample. Scans were made from 400–7000 cm^{-1} with a resolution of 4 cm^{-1} and averaged over 64 scans. Optical artifacts were removed and the absorption spectra were corrected using methods previously described in detail elsewhere.[133,134] Due to the BeO film being deposited on an IR-opaque highly *p*-doped Si substrate, reflectance FTIR spectra were instead collected for this film using a germanium attenuated total reflection (GATR) attachment and the same FTIR spectrometer.[135] GATR spectra were collected from 650–4000 cm^{-1} with a resolution of 4 cm^{-1} and averaged over 256 scans.

To check for the presence of crystallinity in the ALD and PEALD high-*k* films, omega-2theta (2θ) grazing incidence X-ray diffraction (GIXRD) measurements were performed using a Bruker D8 Discover high-resolution, triple-axis X-ray diffractometer operated at 40 kV (Cu-Kα, λ = 1.5418 Å).[136] In order to increase the diffraction volume for thin films, an incident angle of 0.5° from the outermost film structures was selected.

The surface morphology/roughness of the ALD films was investigated by atomic force microscopy (AFM) using a Bruker Dimension Icon operating in PeakForce tapping mode. The samples were imaged using a ScanAsyst tip with a peak force setpoint of 275 pN. The imaging speed was 0.3 Hz with the noise threshold set to 0.3 nm. The root mean square (RMS) surface roughness was calculated over a 10 × 10 micron image of the AFM surface height collected from several regions of each sample.

Film thickness, optical, and electrical property characterization.—
Film thickness and refractive index were determined by spectroscopic ellipsometry using a J. A. Woollam variable angle spectroscopic ellipsometer (VASE).[125] Five different incident angles (55, 60, 65, 70, and 75°) were utilized to collect reflectance in the 600–1000 nm wavelength range where the extinction coefficient for the high-*k* dielectrics was negligible. The Woollam

software was then utilized to deduce the thickness and refractive index (RI) as a function of wavelength. The specific refractive indexes for the investigated high-*k* films are reported at a wavelength of 673 nm.

The electrical and dielectric properties of the high-*k* dielectric films were investigated by IV and CV measurements using a previously described Hg prober.[136] More specifically, the low-frequency dielectric constant (*k*) was determined by metal−insulator−semiconductor (MIS) CV measurements performed at 0.1–1 MHz. The leakage currents were determined by separate IV measurements performed using the same MIS structures and Hg probe system. A compliance current of 10^{-4} A ($\sim 4 \times 10^{-3}$ A/cm^2) was set for the IV measurements and used to define the dielectric breakdown for instances in which a steep (several decade) increase in leakage current is not observed.

Mechanical property characterization.—The Young's modulus (*Y*) and hardness (*H*) for the 100–200 nm thick high-*k* films were determined by nanoindentation using a Berkovich cube corner diamond tip and a Hysitron Triboindenter with a load range up to 4 mN.[137] Each sample was tested at ten locations. Depth-dependent properties were examined by performing multiple load/unload cycles at different indentation loads. The film modulus was then calculated using the depth-dependent apparent modulus via linear extrapolation.[138] To determine the film stress for the high-*k* films, pre- and post-deposition scans of the Si substrate wafer were performed using a previously described laser deflection method.[139,140] The change in wafer curvature was then utilized to calculate film stress using Stoney's formula and the optically determined film thickness.[141]

Thermal property characterization.—*Coefficient of thermal expansion.—*The in-plane CTE for the Al$_2$O$_3$, AlN, and HfO$_2$ high-*k* dielectrics was measured using a Frontier Semiconductor TC900 laser stress measurement system. Specifically, this tool was utilized to monitor changes in the high-*k*/Si wafer curvature as a function of temperature using a laser deflection system previously described.[139,140] The change in wafer curvature was used to calculate CTE using Stoney's formula and previously described methods.[139–141] For the measurements reported here, the change in radius of curvature while heating from 23−400°C in a $< 10^{-5}$ Torr vacuum was measured using 200 nm thick high-*k* films deposited on Si. The maximum temperature of 400°C was selected as this was slightly above the deposition temperature for the films and is generally the maximum temperature allowed in metal interconnect fabrication.[119] The heating rate was 5°C/min and the cooling rate approximately 10°C/min. The samples remained at the target temperature of 400°C for 5 minutes before cooling. The radius of curvature was monitored upon heating and cooling for two cycles. To calculate the CTE of the high-*k* films, the CTE of the Si substrate (α_s) was taken to be 2.6°C/part per million (ppm), and the high-*k* Young's modulus determined by nanoindentation measurements was used.[140] The Poisson's ratio (ν_f) for Al$_2$O$_3$, AlN, and HfO$_2$ were assumed to be 0.23,[142] 0.25,[143] and 0.25,[144] respectively, based on their bulk values.

The out-of-plane CTE for the ALD BeO, Al$_2$O$_3$, and HfO$_2$ films was determined via X-ray reflectivity (XRR) thickness measurements performed between room temperature and 400°C. The details of these measurements have been described previously.[140,145] Briefly, the XRR measurements were carried out on a Bruker D8 Discover diffractometer (Cu *K*α radiation, λ = 0.15418 nm) equipped with a DHS 900 domed hot stage attachment. An equilibrium period of 90 minutes was found to be optimal for both the sample and stage to stabilize at the temperature of interest. After stabilizing at each temperature, sample alignment was carried out using a routine whereby the sample height and angle were iteratively checked and adjusted relative to the X-ray radiation. A θ–2θ configuration was adopted for the XRR scan, with θ scanned from 0° to 3.0° with a step size of 0.001° and a counting time of 1 second/step for a total scan time of 50 minutes. Data were collected at 40 kV and 40 mA.

Values for the out-of-plane CTE for the ALD films were obtained by analyzing the films' temperature-dependent thicknesses, calculated

from the XRR measurements. The XRR Modeling program BEDE Refs v4.00 was used to fit the critical angle and Kiessig fringes of each XRR pattern, yielding the total film thickness and density of each sample.[145] Reflectivity measurements are highly sensitive to correct sample alignment, and several alignment and measurement cycles were used to determine a baseline uncertainty in thickness as determined from XRR. For all films, the standard deviation in thickness between several measurements was on the order of 0.015 nm. For the case of measuring the CTE, thicker films, larger CTE values, and larger ΔT reduce the uncertainty due to the instrumental error resulting from imperfect sample alignment. As described previously,[145] the CTE of the films were determined from the change in thickness with temperature, however, a slope calculated from thickness (d) at several temperatures (T) was used as opposed to Δd and ΔT values obtained from two endpoints. The reported error in CTE for out-of-plane measurements corresponds to CTEs calculated from the 95% confidence interval in the linear regression fit to these data. Calculations of the CTE were made assuming the same value of α_s in the in-plane CTE measurements and $\nu_f = 0.2$, 0.23, and 0.25 for BeO,[124] Al_2O_3,[142] and HfO_2,[144] respectively.

Thermal conductivity.—The out-of-plane thermal conductivity and interfacial thermal resistance between the ALD high-k dielectrics and the Si substrate was determined via TDTR measurements that have been previously described.[58,146] Briefly, an aluminum film with nominal thickness of 80 nm was first deposited on the ALD high-k dielectrics via E-beam evaporation. The samples were then exposed to a short (<1 ps) pulsed optical beam from an oscillating Ti:sapphire laser operating at a repetition rate of 80 MHz centered at a wavelength of 800 nm. The fundamental output of the laser was split into a pump beam, frequency doubled to 400 nm, and a probe beam, which were subsequently focused on the Al-coated sample with respective approximate diameters of 60 and 20 μm. Before being focused onto the area of interest, the probe beam was directed to a translation stage, which allowed the arrival of the probe pulses, with respect to the pump pulses, to be delayed by up to six nanoseconds with sub-picosecond resolution. An electro-optical modulator modulates the pump beam in order to produce a modulated thermal event in the aluminum film that decays into the sample. In this manner, changes in the reflectivity of the Al coated samples induced by the modulated pump beam were measured by the probe beam. In order to determine the cross-plane thermal conductivity and interfacial thermal resistance, the temperature-dependent change in reflectivity was modeled using previously described methods.[147,148] This simulation requires both the Al film thickness and heat capacity of the high-k dielectric. The former was determined via both mechanical profilometry as well as picosecond acoustics, the details of which have been described thoroughly elsewhere.[58] For the latter, the heat capacity reported for bulk high-k dielectrics were utilized and scaled by the density as measured via NRA-RBS.[149,150] As will be discussed later, this assumption was justified based on the mass density of the high-k films approaching the bulk crystalline values.

Results

Elemental composition.—Table I summarizes the NRA-RBS elemental and mass density analysis for the investigated high-k films. For comparison, results are also included for a thermally grown SiO_2 film and a common PECVD SiN:H etch stop/passivation film.[126,151] The oxide films all have low carbon (< 2%) and hydrogen (0.1–7%) impurities. The 1–2% C in the ALD BeO and Al_2O_3 films is consistent with the metal–organic precursors used to deposit the films (TEB and TMA, respectively). Several prior studies of ALD Al_2O_3 have shown the incorporation of carbon impurities to be sensitive to both the deposition temperature and choice of precursors and oxidants.[152,153] The low hydrogen content for the BeO and HfO_2 high-k films is consistent with their measured mass densities being close to or equivalent to the theoretical densities of their crystalline counterparts.[124,126,144] The oxygen/cation ratios of 1.05 and 1.9 for the BeO and HfO_2 films, re-

spectively, are also consistent with the expected stoichiometry. However, the O/Al ratio for the ALD Al_2O_3 film in this study of 2.0 is significantly higher than the expected value of 1.5. This indicates that the ALD Al_2O_3 film is off-stoichiometric and oxygen rich. Hemmen has shown previously for low temperature (<100°C) films that high oxygen content can be attributed to the incorporation of OH groups into the Al_2O_3 film.[28] The association of OH and oxygen-rich stoichiometries is likely due to OH incorporation as (AlO)OH as in Boehmite.[154,155] However, the Al_2O_3 film in this study was deposited at higher temperatures (>300°C) and has a low hydrogen content of ~1%. An alternative and more likely explanation is that ALD growth of the Al_2O_3 film in this study utilized undersaturated TMA exposures. For PEALD Al_2O_3 growth, Langereis has previously shown that this undersaturation can result in the growth of low-hydrogen-content, oxygen-rich films.[156]

The AlN film exhibits undetectable levels of O and C, but a significant amount of hydrogen at 15.5%. This level of hydrogen is consistent with the mass density of the PEALD AlN film being reduced at 2.7 g/cm³ relative to the theoretical crystalline density of wurtzite AlN at 3.2 g/cm³.[143] Interestingly, these values are comparable with those shown for PECVD SiN in Table I and are consistent with the results of other PEALD AlN investigations where films with mass densities of 2.0–2.8 g/cm³ and hydrogen contents of 13–27% have been reported.[157–159] Bosund in particular has previously shown that PEALD AlN hydrogen content and mass density are both a strong function of growth temperature and nitrodizing plasma time with hydrogen content decreasing with increasing temperature and plasma time, while mass density shows the opposite dependence.[157]

Similar to the ALD Al_2O_3 film, the N/Al ratio for the PEALD AlN film is slightly above the expected stoichiometric value (1.2 vs. 1.0), indicating that this film is also slightly off-stoichiometric and nitrogen-rich. This is again consistent with prior studies by Bosund and others.[157–159] However, Motamedi has recently reported the growth of Al-rich PEALD AlN films.[160,161] This difference may be due to the use of a N_2-5% H_2 plasma versus the NH_3 plasma utilized in the Bosund study or due to differences in the two techniques utilized to measure the elemental composition (surface-sensitive X-ray photoelectron spectroscopy (XPS) was used by Motamedi versus bulk-sensitive RBS for Bosund and other studies[157–159]). In either case, the nitrogen-rich stoichiometry and presence of significant amounts of hydrogen detected for the PEALD AlN film in this study suggests the excess nitrogen may be incorporated primarily as NH_x groups. The presence of such groups will be confirmed by FTIR measurements to be presented next.

Atomic/nano-structure.—To better understand the chemical bonding and origin of the non-stoichiometry in the ALD Al_2O_3 and PEALD AlN films, transmission FTIR spectra were acquired from both films as shown in Figure 1. The ALD Al_2O_3 T-FTIR spectrum (Fig. 1a) shows only a broad absorption band centered at ~755 cm⁻¹ that is similar in appearance to other reported FTIR spectra for Al_2O_3 films deposited by ALD[162–164] and PECVD[165–167] methods. The broad nature of the absorption band shown in Fig. 1a is generally attributed to unresolved Al–O–Al bending (650–700 cm⁻¹) and Al–O stretching (750–850 cm⁻¹) bands.[162–167] Alternatively, the Al_2O_3 FTIR absorption band in this range can be interpreted in terms of the Al coordination where the stretching modes for AlO_6 octahedra are expected at 500–750 cm⁻¹ whereas the stretching modes for AlO_4 tetrahedra are expected at 750–850 cm⁻¹.[154,155] From this perspective, the broad nature for the Al–O absorption band in Fig. 1a suggests a mix of four- and six-fold coordinated Al for the ALD Al_2O_3 film. However, we note that in AlOOH (Boehmite) ceramics this absorption band is typically split into three components that may be related to Al–O–Al and Al–O–O stretching motions for Al in both four- and six-fold coordination.[154] This latter interpretation is more consistent with the previously noted oxygen-rich stoichiometry observed by NRA-RBS.

In contrast to the ALD Al_2O_3 film, the T-FTIR spectrum (Fig. 1b.) for the PEALD AlN film shows a much sharper absorption band at ~670 cm⁻¹ that is similar in appearance to other reported FTIR

Table I. Summary of NRA-RBS elemental composition and mass density (ρ), as well as AFM RMS surface roughness for the ALD and PEALD high-*k* dielectrics investigated in this study. For reference, results for a thermally grown SiO₂ and a plasma-enhanced chemically vapor deposited SiN:H film are included as well.[126,151]

Film	% Cation*	% C	% N	% O	% H	ρ (g/cm³)	RMS (nm)
BeO	45 ± 3 (Be)	3 ± 1	0	48 ± 3	4 ± 1	3.0 ± 0.3	10.0 ± 0.1
Al₂O₃	33 ± 2 (Al)	1 ± 1	0	65 ± 5	1 ± 1	3.0 ± 0.1	0.3 ± 0.1
HfO₂	32 ± 2 (Hf)	1 ± 1	0	61 ± 4	7 ± 1	9.8 ± 0.3	3.0 ± 0.1
AlN	38 ± 3 (Al)	0	47 ± 3	0	15 ± 1	2.7 ± 0.1	5.3 ± 0.1
SiN:H	39 ± 3 (Si)	0	38 ± 3	1 ± 1	22 ± 2	2.6 ± 0.1	0.4 ± 0.1
SiO₂	34 ± 2 (Si)	0	0	66 ± 5	0	2.2 ± 0.1	0.2 ± 0.1

*The uncertainty in the measured elemental contents is approximately 0.05 times the measured content for that element. Error propagation typically leads to a 6 to 7 percent uncertainty when the absolute contents (in atoms/cm²) are expressed in atomic percent.

spectra from PEALD,[161,168] PECVD,[169,170] CVD,[171] and sputter[172,173] deposited AlN films. The absorption band at 670 cm⁻¹ in AlN materials is generally attributed to the four fold-coordinated Al–N stretching mode.[161] In crystalline wurtzite AlN, this absorption band corresponds more specifically to the transverse optical (TO) phonon mode with the longitudinal optical (LO) mode occuring at ∼916 cm⁻¹.[174] Although more detailed peak deconvolution was not attempted for the Al–N band, both the TO and LO modes are likely present in the FTIR spectrum shown in Fig. 1b. The full width at half maximum (FWHM) for the LO mode has been previously correlated to the degree of order in amorphous and poly-crystalline AlN films as well as other properties such as thermal conductivity which will be discussed in more detail later.[168,173]

In addition to the Al–N band, the T-FTIR spectrum for the PEALD AlN film also shows smaller absorption bands at 2110 and 3200 cm⁻¹ that are related to Al–H and N–H stretching modes, respectively.[170] The clear presence of these absorption bands in the PEALD T-FTIR spectrum is consistent with the significant amount of hydrogen detected by NRA-RBS in this film. The absence of similar hydrogen-related absorption bands in the ALD Al₂O₃ film is also consistent with the hydrogen content in this film being near the detection limits of NRA-RBS. The presence of the N–H$_x$ absorption band in the PEALD AlN FTIR spectrum is also consistent with the nitrogen-rich stoichiometry observed in the NRA-RBS measurements and the previous supposition that some of the excess nitrogen is present as NH$_x$ species.

Additional T-FTIR and GATR measurements were performed on the BeO and HfO₂ films. For HfO₂ (see Fig. 1c.), absorption bands at 405, 510, and 600 cm⁻¹, consistent with the Hf–O stretching modes
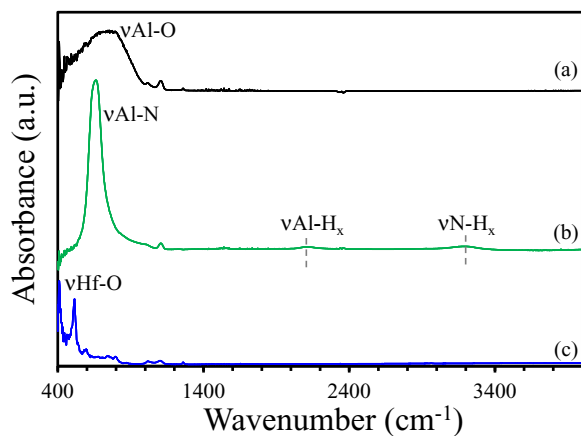
in monoclinic HfO₂, were observed and no hydrogen-related absorption bands were detected.[175,176] Similarly for BeO (see Fig. 2), a Be–O stretching mode was observed at ∼800 cm⁻¹ just above the 650 cm⁻¹ GATR detector threshold,[177] but no hydrogen-related absorption bands were observed.[178] In both cases, the lack of observable hydrogen-related absorption bands is consistent with the low levels of hydrogen detected in these films by the NRA-RBS measurements. The observation of Hf–O stretching modes attributed to the monoclinic HfO₂ phase does suggest the possible presence of some crystallinity for the ALD HfO₂ film, which will be more clearly demonstrated next.

To determine whether the high-*k* films were amorphous or crystalline, XRD measurements were also performed. For the ALD Al₂O₃ and PEALD AlN films, no X-ray diffraction peaks were observed and the films were thus concluded to be X-ray amorphous. This is consistent with several other XRD and transmission electron microscope (TEM) investigations of ALD and PEALD Al₂O₃ where amorphous films have been routinely reported.[18,66,164] In contrast, prior investigations of PEALD AlN have reported the growth of both amorphous[157,158] and poly-crystalline[161,179] films. In this regard, we note that the stoichiometry for previously studied amorphous PEALD AlN films has been reported to be nitrogen-rich,[157,158] which is consistent with our observations. Poly-crystalline PEALD AlN films, however, have been reported to have aluminum-rich stoichiometries.[161,179] While various growth conditions may be important in controlling the stoichiometry, this observation suggests that crystallinity in PEALD AlN is perhaps a function of stoichiometry.

For the BeO and HfO₂ films, X-ray diffraction peaks consistent with the wurtzite BeO[122] and monoclinic HfO₂[175,176] crystalline phases were detected, respectively. These observations are consistent with both films exhibiting low impurity levels, ideal stoichiometry, and mass densities close to their theoretical crystalline values.[124,144] They

Figure 1. Transmission FTIR spectra of (a) ALD Al₂O₃, (b) PEALD AlN, and (c) ALD HfO₂. Note: the small unlabeled peak at ∼1110 cm⁻¹ is an artifact produced due to differences in the amount of substitutional oxygen present in the thin film Si substrate and the background Si substrate utilized in the FTIR measurements.
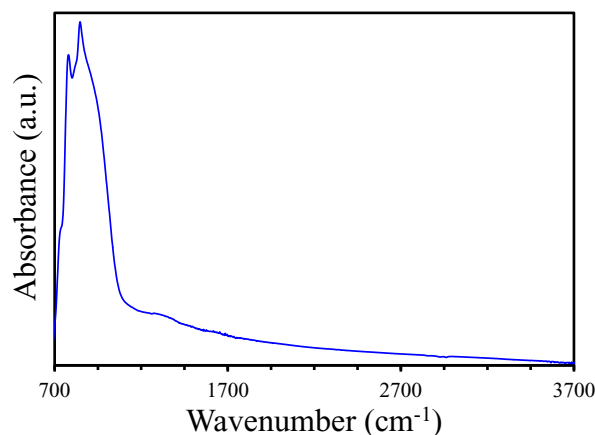

Figure 2. GATR spectrum of ALD BeO illustrating Be-O stretching mode at ∼800 cm⁻¹.
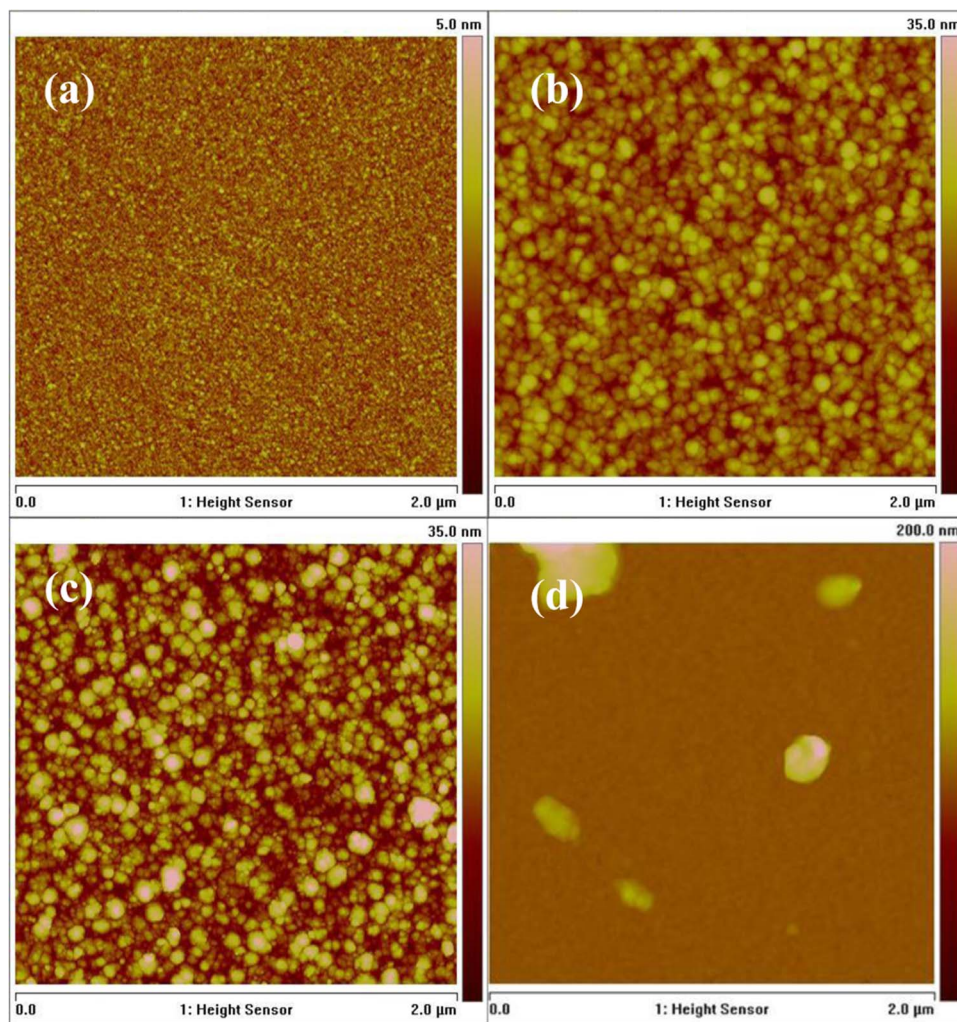
Figure 3. AFM surface height maps for (a) ALD HfO$_2$, (b) ALD Al$_2$O$_3$, (c) PEALD AlN, and (d) ALD BeO.

are also consistent with prior XRD and TEM investigations where epitaxial growth of BeO on Si has been reported,[122,123] and the growth of mixed amorphous/nano-crystalline HfO$_2$ films on Si has also been reported.[60,180,181] For the latter, we note that in some cases the degree of crystallinity in ALD HfO$_2$ has been observed to increase with thickness/number of growth cycles,[18,30,56] and that other tetragonal and orthorhombic crystalline phases have been reported.[180,181] Post-deposition annealing at 500–900°C has been additionally shown to crystallize or improve the crystallinity of ALD or PEALD deposited HfO$_2$,[93] BeO,[122] and AlN[158] films. In contrast, amorphous ALD/PEALD Al$_2$O$_3$ films have proven more difficult to crystallize via post-deposition annealing with temperatures of 800–1000°C typically being required to observe crystallization.[182,183]

To further investigate the nano-structure of the ALD high-k films, AFM was utilized to look at the surface morphology. Figure 3 shows 2 × 2 micron AFM surface height images for each of the high-k films investigated in this study. For better comparison to other literature reported values, the RMS surface roughnesses summarized in Table I were determined from larger 10 × 10 micron images of the same samples. The ALD BeO and AlN films exhibited high RMS surface roughnesses of 10 and 5.3 nm, respectively. For the ALD BeO film, the high surface roughness was primarily due to the presence of small surface particles which may be evidence of either gas phase nucleation during ALD growth or BeO crystallite formation during the post deposition rapid thermal anneal. While AFM measurements were not performed on the ALD BeO sample prior to RTA, we do note that such surface particles were not observed on other unannealed ALD

BeO films in a prior investigation.[124] Excluding the surface particles, the calculated RMS surface roughness is reduced to 1 nm, closer to measured roughness values for the other high-k films. We also note that prior AFM measurements of thinner (3–5 nm) amorphous BeO films grown on GaAs show an RMS roughness of < 0.2 nm.[123,184]

Concerning the PEALD AlN film, the RMS surface roughness of 5.3 nm is slightly higher than, but consistent with, the RMS surface roughness values reported by Bosund for TMA/NH$_3$ PEALD AlN. Specifically, Bosund observed that the RMS surface roughness increased from 1 to 2.8 nm as the growth temperature increased from 100 to 300°C.[157] Ozgit has similarly shown for TMA/NH$_3$ PEALD AlN that the AFM RMS surface roughness for a 2 × 2 micron scan also increases from 0.3 to 1.4 nm as the film thickness increases from 33 to 100 nm.[179] Thus, the high surface roughness for our PEALD AlN film can be partially attributed to the high deposition temperature and the comparatively high thickness of 200 nm. It is also interesting to compare the RMS roughness for the PEALD AlN film to that observed for PECVD SiN:H. In this case, the RMS surface roughness of 5.3 nm for the PEALD AlN film is substantially higher than the value of 0.4 measured for the PECVD SiN:H comparison film in this study. Since the RF power utilized in the plasma-activated nitrodizing step during AlN PEALD is similar to that utilized during SiN:H PECVD, this indicates that the high surface roughness of the PEALD AlN film cannot be explicitly attributed to the addition of the plasma activation step.

With regard to HfO$_2$, we note that Gieraltowska has previously shown that the AFM surface roughness of ALD HfO$_2$ grown at 85°C

Table II. Summary of electrical and optical properties for the ALD and PEALD high-k dielectrics investigated in this study. For comparison, results for a thermally grown SiO_2 and PECVD SiN:H film are included from prior investigations.[125,126,228]

Film	RI (± 0.01)	k_{HF} (> 1 THz)	k_{LF} (100 kHz)	J (A/cm^2 @ 2 MV/cm)	E_{bd} (MV/cm)	E_g (eV)
BeO	1.71	2.9	7.5 ± 0.2	9×10^{-8}	>6–10	8.0 ± 0.2[126]
Al_2O_3	1.66	2.8	6.5 ± 0.2	3×10^{-9}	>10	6.0 ± 0.2[126]
HfO_2	2.09	4.4	25.0 ± 1	3×10^{-8}	>7	5.5 ± 0.2[126]
AlN	1.95	3.8	8.0 ± 0.2	7×10^{-8}	>5	6.1 ± 0.5[228]
SiN:H	2.01	4.0	6.5 ± 0.1	1×10^{-8}	>5	3.2 ± 0.2[125]
SiO_2	1.40	2.0	3.9 ± 0.1	2×10^{-9}	>10	8.8 ± 0.2[228]

RI = refractive index, k_{HF} = high-frequency/optical dielectric constant (=RI^2), k_{LF} = low-frequency dielectric constant, E_{bd} = dielectric breakdown field, and E_g = bandgap.

using $Hf[(CH_3)_3N]_4/H_2O$ increases from 0.3 to 6 nm as film thickness increases from 20 to 200 nm for a 10 × 10 micron scan.[18] Similarly, increasing the growth temperature from 85 to 350°C for a 100 nm thick HfO_2 film increased the surface roughness from 1 to 2.9 nm. These surface roughness values are fully consistent with the RMS surface roughness of 3.0 nm obtained for the ALD HfO_2 film in this study.[18] Interestingly, more detailed studies by Hausmann have shown that the increased surface roughness for ALD HfO_2 is the result of nano-crystallite formation in what begins as an amorphous HfO_2 film.[180] The increased crystallite nucleation and the faster growth rate for the crystallite relative to the amorphous film leads to increased surface roughness as film thickness increases. Thus, the combined AFM and XRD measurements suggest that the BeO and HfO_2 films consist of nano-crystalline regions embedded in an amorphous matrix film.

The ALD Al_2O_3 film had the lowest RMS surface roughness of 0.3 nm. This is consistent with several prior investigations where values of <0.4 nm have been generally reported for a similar 10 × 10 micron scan window.[60,62] Interestingly, Tapily has previously directly compared ALD Al_2O_3 and HfO_2 films and found HfO_2 to generally be about 30 times rougher than Al_2O_3.[60] The low roughness for ALD Al_2O_3 at high thickness and growth temperature can likely be attributed to the strong resistance to crystallization this material exhibits.[182,183] This would be consistent with the very low roughness observed in this study for the thermal oxide, which is another material that is difficult to crystallize.[185]

Electrical and optical properties.—Table II summarizes the electrical and optical properties for the investigated high-k films. From the VASE measurements, BeO and Al_2O_3 have similar RI values of ~1.66–1.70 while AlN and HfO_2 have significantly higher RI values of 1.95 ± 0.01 and 2.09 ± 0.01 respectively. These values correlate well with the low-frequency dielectric constants determined from the Hg probe CV measurements, where BeO and Al_2O_3 were found to have k values of 7.5 ± 0.2 and 6.5 ± 0.2, respectively, while AlN and HfO_2 displayed higher k values of 8 ± 0.2 and 25 ± 1 respectively. While these results are likely specific to the growth conditions utilized, we do note that similar values have been reported for ALD, PEALD, CVD, and sputter deposited Al_2O_3 (RI = 1.6–1.7, k = 6–9),[28,58,186–189] HfO_2 (RI = 1.85–2.05, k = 14–22),[18,190,191] AlN (RI = 1.8–2.2, k = 5.7–9.5),[84,86,88,97–101] and BeO films (RI = 1.67–1.72, k = 6.5–6.8).[184,192] Relative to SiO_2, all the investigated dielectrics have substantially higher values of RI and k. Relative to SiN:H, however, only HfO_2 has a significantly higher RI and k.

As the square of the RI represents the high-frequency dielectric constant of a material,[193] it is interesting to compare the high- and low-frequency dielectric constants for the various high-k films. For BeO, Al_2O_3, and AlN the high-frequency dielectric constant (RI)^2 is roughly 40–50% of the low-frequency dielectric constant whereas for HfO_2, RI^2 is only 20% of the low-frequency dielectric constant. Since the high-frequency dielectric constant represents only electronic contributions to dielectric permittivity and the low-frequency dielectric constant includes electronic, ionic, and configurational contributions,[193] the higher low-frequency dielectric constant for HfO_2 points toward

essentially complete ionic bonding and possibly some configurational contributions.[4] This is consistent with the significant covalent bonding character reported for BeO, AlN,[194,195] and, to a lesser degree, Al_2O_3.[8]

Figure 4 presents the leakage current density (J) measured for the high-k films as a function of electric field (E) in comparison to thermally grown SiO_2 and PECVD SiN:H. As summarized in Table II, all the films exhibit a low leakage current (<1×10^{-7} A/cm^2) at a modestly high electric field of 2 MV/cm and a high breakdown strength (>5 MV/cm), consistent with numerous reports of the electrical properties of these materials.[18,159,184,190] However, the field dependence of the leakage current and breakdown characteristics differed amongst the materials. Specifically, AlN, BeO, and SiN:H exhibited a near continuous increase in electrical leakage up to the compliance current set for the IV measurements (10^{-4} A). In contrast, SiO_2, Al_2O_3, and HfO_2 exhibited essentially field independent leakage up to electric fields of 3–6 MV/cm followed by a gradual rise in leakage and then a sharp step function increase up to the compliance current. It is also interesting to note that AlN and SiN:H exhibited similar breakdown strengths (E_{bd}) of ~5.7 MV/cm, while the oxides such as BeO, Al_2O_3, and SiO_2 exhibited much higher E_{bd} of 10–12 MV/cm with HfO_2 in between at ~7.5 MV/cm. This contrasting behavior in E_{bd} and leakage current field dependence can be attributed to differences in electron transport mechanisms, bond type, and electronic structure (bandgap, E_g).

Regarding the leakage current field dependence, numerous studies of electron transport in SiO_2, SiN:H, and high-k gate dielectric materials have reported a wide variety of transport mechanisms ranging from bulk-limited processes such as space-charge-limited conduction,[196] ion/impurity conduction,[197] defect mediated (Poole–Frenkel)[198] conduction, and trap-assisted tunneling (TAT),[199] to interface limited processes such as Schottky emission and Fowler–Nordheim tunneling.[200]
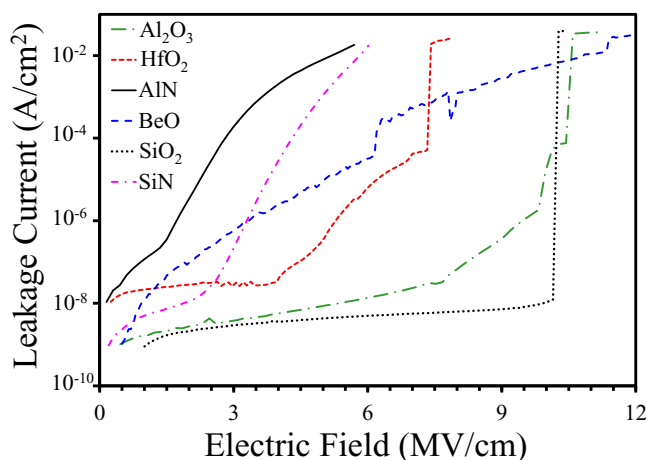
Figure 4. IV measurements for ALD Al_2O_3, HfO_2, BeO, PEALD AlN, thermal SiO_2, and PECVD SiN:H.

For relatively thick (100 nm to 1 μm) SiN films, such as in this study, numerous prior investigations have reported bulk Poole–Frenkel (PF) trap/defect-mediated conduction to be the dominant leakage transport mechanism.[201–204] Interestingly, recent investigations of the electrical properties of sputter deposited and PEALD AlN have also reported electrical leakage to occur predominantly by the PF mechanism.[205–207] More recent electrically detected magnetic resonance (EDMR) measurements by Mutch et al. have conclusively shown that electron transport in PECVD SiN:H specifically occurs through silicon dangling bond defect states located in the mid-upper portion of the SiN bandgap.[208,209] Owing to the similar IV characteristics, deduced leakage mechanism, and band structure,[210] it seems plausible that electron transport in amorphous AlN (independent of deposition method) may also occur through Al dangling bond defect states. However, first principles density functional theory calculations for the band structure of AlN have so far indicated the lack of such midgap states.[210,211]

In contrast to SiN and AlN, electrical leakage through SiO$_2$ has been reported to be interface-limited and to occur via either Fowler–Nordheim (FN)[200,212] or trap-assisted-tunneling (TAT).[213,214] This difference can be partially attributed to the ultra-low defect densities[215] typically achieved in gate-dielectric-quality SiO$_2$ and the two times larger bandgap for SiO$_2$ ($\sim$9 eV)[216] relative to Si$_3$N$_4$ ($\sim$5.5 eV).[217] Interestingly, TAT and FN tunneling have also been reported as the dominant leakage mechanisms in a number of investigations of the electrical properties for Al$_2$O$_3$ films deposited by a variety of methods.[188,218–220] This is consistent with the similar IV characteristics exhibited by the thermal SiO$_2$ and ALD Al$_2$O$_3$ films in Fig. 4.

In contrast to the electrical behavior for SiO$_2$ and Al$_2$O$_3$, the high field electrical leakage mechanism for HfO$_2$ has been primarily reported to be of PF nature.[221–224] This is consistent with the general appearance of the HfO$_2$ IV trace in Fig. 4 differing from that for Al$_2$O$_3$ and SiO$_2$. Excluding the breakdown region (which will be discussed later), PF leakage for HfO$_2$ is also consistent with the HfO$_2$ IV curve in Fig. 4 resembling a stretched version of that for AlN and SiN:H where, as previously mentioned, PF leakage has also been determined by consensus. PF leakage can be more definitively ascertained directly from IV measurements via plotting the results as ln(J/E) vs $E^{1/2}$. If the plot is linear, the slope for PF transport should equate to $(q^3/\pi\varepsilon_0\varepsilon_r)^{1/2}(kT)^{-1}$ where q is the electron charge, ε_0 is the permittivity of free vacuum, ε_r is the high frequency dielectric constant, k is Boltzman's constant, and T is temperature.[223] Such a plot for the high field portion of the HfO$_2$ IV curve (3.8–7 MV/cm) is indeed linear with a slope that indicates a high frequency dielectric constant of 8.0, in fair agreement with the optical dielectric constant (RI^2) of 4.4 determined by the VASE measurements (see Table II). For the SiN:H and AlN data shown in Fig. 4, similar plots resulted in linear curves and indicated high-frequency dielectric constants of 3.9 and 7.0, respectively. The former is in excellent agreement with the VASE optical dielectric constants (RI^2) of 4.0 for SiN:H, whereas the latter is again in fair agreement with the RI^2 of 3.8 for AlN (see Table II). In this regard, we do note that the optical dielectric constant was calculated based on the RI reported at a wavelength of 673 nm. As RI generally increases with decreasing wavelength,[225] utilizing a shorter wavelength RI to calculate the high-frequency optical dielectric constant would bring the two measurements of the high-frequency dielectric constant into closer agreement. Still, the fair agreement between VASE RI^2 and the dielectric constant deduced by PF analysis for AlN and HfO$_2$ suggests that electrical leakage in these two specific films may not be purely PF.

For BeO, the IV curve does not closely resemble that for any of the other dielectrics in Fig. 4 and, to the authors' knowledge, no detailed investigations of the leakage mechanisms in BeO have been previously reported. In an attempt to ascertain the mechanism, the BeO IV data was also plotted as ln(J/E) vs $E^{1/2}$. While linearity was observed over a wide range of electric field (2–6 MV/cm), the high frequency dielectric constant deduced from the slope was 42, much higher than the VASE optical dielectric constant of 2.9. Another possibility is Schottky emission (SE) based leakage which would also exhibit linearity in a ln(J/E) vs $E^{1/2}$ plot, but with a slope two times
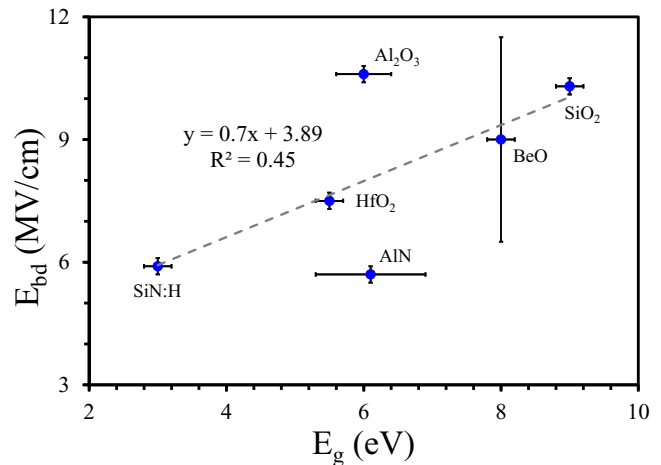

Figure 5. E_{bd} vs. E_g correlation for ALD Al$_2$O$_3$, HfO$_2$, BeO, PEALD AlN, Thermal SiO$_2$, and PECVD SiN.

higher than that predicted for PF conduction.[198] Assuming SE leakage instead, we deduced a high frequency dielectric constant of 10.6 which is closer to but still substantially higher than the observed optical dielectric constant. Thus, it is unlikely that electrical leakage in ALD BeO is strictly PF or SE and is more likely some other mechanism such as TAT or some combination of mechanisms that requires more complex analysis that is beyond the scope of this study.

Concerning E_{bd}, we note that the values summarized in Table II are consistent with other reports,[18,28,189,203,226,227] and scale roughly with previously reported reflection electron energy loss spectroscopy (REELS) bandgap (E_g) measurements performed on identical materials (see Fig. 5).[124–126,228] This is consistent with recent combined DFT calculations and machine learning algorithms by Kim which have shown that the intrinsic breakdown strength of a dielectric material is exponentially proportional to the square root of the product of the material's E_g and the phonon cutoff frequency (ω_{max}).[229,230] We do note that the correlation between E_{bd} and E_g shown in Fig. 5 is not strong with an R^2 of only 0.45. The two main outliers are AlN and Al$_2$O$_3$. In this regard, we note that the bandgap reported for the AlN film may have been overestimated due to the surface sensitivity of REELS and the presence of an unavoidable native AlO$_x$ surface with a bandgap of $\sim$6 eV.[228] This would be consistent with the REELS measurements of the ALD Al$_2$O$_3$ film which also showed E_g $\sim$6 eV. It would further be consistent with optical measurements, which are not sensitive to surface oxides, that have indicated bandgaps ranging from 4 to 6 eV for amorphous AlN films deposited by a variety of methods with varying stoichiometry.[231,232] In particular, Gordon has reported bandgaps of 5.0–5.5 eV for amorphous CVD AlN films with similar compositions to the PEALD AlN film in this study.[232] Thus, it is possible that the bandgap for the PEALD AlN film in this study is substantially lower which would improve the E_{bd} vs. E_g correlation.

Concerning the other partial outlier in Fig. 5, we note that it is possible that the bandgap for the ALD Al$_2$O$_3$ film is slightly underestimated for similar reasons to AlN. Specifically, the presence of surface defects or hydroxyl species could make the E_g determined by REELS for ALD Al$_2$O$_3$ appear reduced relative to the bulk value.[126] We also note that REELS measurements of PEALD Al$_2$O$_3$ and other EELS measurements of ALD and PEALD films have indicated slightly higher bandgaps in the 6.5–7.0 eV range.[233–235] Further, the bandgap for single crystal Al$_2$O$_3$ (sapphire) is closer to 8 eV.[126] Thus, it is possible that the bandgap for the ALD Al$_2$O$_3$ film in this study is slightly higher than indicated by REELS which would further improve the E_g vs. E_{bd} correlation. We do note that for SiN:H, SiO$_2$, HfO$_2$, and BeO the REELS bandgaps are in strong agreement with other REELS and optical measurements.[124–126] The REELS results for SiO$_2$ and HfO$_2$ are also in strong agreement with the reported bandgaps for their crystalline counterparts.[216,236] Lastly, McPherson has shown that

Table III. Summary of thermal and mechanical properties for the ALD and PEALD high-*k* dielectrics investigated in this study along with representative values for PECVD a-SiN:H and thermally grown SiO$_2$.

Film	Y (GPa)	H (GPa)	Stress (MPa)	IP CTE (ppm/°C)	OOP CTE (ppm/°C)	κ (W/mK)	ITR (m^{2}K/GW)
nc-BeO	$\geq$330	$\geq$33	NM	NM	6.0 ± 0.1	14.7 ± 3	11.8 ± 0.2
BeO	330 ± 30[124]	33 ± 5[124]	NM	NM	6.0 ± 0.1	10.8 ± 1.7	11.7 ± 0.6
Al$_2$O$_3$	172 ± 8	16 ± 2	278 ± 20	3.8 ± 0.1	2.1 ± 0.2	1.9 ± 0.2	5.8 ± 1.5
HfO$_2$	177 ± 5	10 ± 1	565 ± 60	4.4 ± 0.1	2.4 ± 0.2	3.6 ± 0.3	28.0 ± 3.4
AlN	200 ± 24	22 ± 4	-2300 ± 300	NM	NM	2.9 ± 0.3	39.5 ± 5.3
SiN:H	201 ± 5	23 ± 1	-650 ± 70	1.2 ± 0.3	1.1 ± 1.1	1.7 ± 0.2	14.5 ± 1.4
SiO$_2$	69 ± 1	9 ± 1	NM	0.5 ± 0.1[290]	NM	1.5 ± 0.1	10.0 ± 0.7

Y = Young's modulus, H = hardness, stress = film stress as determined by wafer curvature measurements, IP = in-plane, OOP = out-of-plane, CTE = coefficient of thermal expansion, ppm = part per million, κ = thermal conductivity, ITR = interfacial thermal resistance with Si (001), NM = not measured.

for high-*k* dielectrics E_{bd} has an approximate $k^{-1/2}$ dependence which could significantly reduce E_{bd} for HfO$_2$ relative to the other dielectric materials independent of E_g.[237]

The steepness/slope of the breakdown event, however, does not correlate as well with bandgap. As noted previously, SiN, AlN, and BeO all exhibit a near continuous increase in leakage current up to the somewhat arbitrarily defined compliance current, whereas HfO$_2$, Al$_2$O$_3$, and SiO$_2$ all exhibit a gradual rise in leakage followed by a sharp step function increase up to the compliance current. In this regard, the observed breakdown signature may be more closely related to the degree of covalent vs. ionic bonding for the different materials.[238] As with the discussion on low- vs. high-frequency dielectric constant, we note that SiN,[239] AlN,[143] and BeO[194] are all materials with significant covalent bond character,[195] whereas HfO$_2$, Al$_2$O$_3$, and SiO$_2$ all have substantially more ionic bonding character.[240] As shown by McPherson,[238] ionic materials are more susceptible to field-induced polar bond stretching and breakage that can contribute to sudden time-dependent dielectric breakdown phenomena not exhibited by pure covalent materials.[237]

Thermal/mechanical properties.—Table III summarizes the thermal and mechanical properties determined for the various high-*k* films investigated in this study including Young's modulus, hardness, film stress, coefficient of thermal expansion, thermal conductivity and interfacial thermal resistance. In the following sections, we present some representative results and analysis from these measurements. The results are discussed and compared both amongst the emerging high-*k* dielectrics and to other important dielectrics utilized in microelectronic devices (e.g., SiN:H and SiO$_2$). To facilitate a broader perspective and understanding of the structure−property relationships in high-*k* materials, the results summarized in Table III are also compared to previously reported results on similar high-*k* films deposited by ALD and other methods as well as values reported for the bulk poly-crystalline and single-crystalline forms of these materials.

Nanoindentation Young's modulus and hardness.—Figure 6 presents a representative plot of indentation modulus as a function of indentation depth for the 200 nm ALD HfO$_2$ film. Based on linear extrapolation to zero indentation depth,[138] the indentation modulus (M) was determined to be 189 ± 5 GPa. Taking Poisson's ratio for the HfO$_2$ film to be 0.25,[144] the Young's modulus ($Y = M(1-\nu^2)$) was calculated to be 177 ± 5 GPa. The results for the other high-*k* and comparison SiO$_2$ and SiN:H films from similar M/Y and H measurements are summarized in Table III. A comparison of Young's modulus and hardness for single-crystalline, poly-crystalline, and amorphous films deposited by other methods for the ALD high-*k* films in this investigation is provided in Table IV.

Of the high-*k* dielectrics investigated, the ALD BeO film has the highest observed nanoindentation Young's modulus and hardness. The value reported in Table III for the annealed partially nano-crystalline BeO film (nc-BeO) is actually a minimum value based on previously reported measurements performed on the unannealed amorphous ALD

BeO film.[124] Unfortunately, the previously mentioned surface particles observed on the annealed ALD BeO film complicated performing the nanoindentation measurements and the interpretation of the results. For this reason, we are only able to state that the Young's modulus and hardness of the annealed nc-BeO film are likely greater than or equal to the values of 330 ± 30 and 33 ± 5 GPa previously reported for the unannealed amorphous BeO film.[124] The high value of Young's modulus for this amorphous/nano-crystalline material, however, is reasonably consistent with the values of 380–420 GPa reported for bulk poly-crystalline and single-crystalline BeO ceramics as shown in Table IV.[241,242]

In decreasing order, the high modulus and hardness exhibited by ALD BeO in this study is followed by PEALD AlN, ALD HfO$_2$, and ALD Al$_2$O$_3$. As shown in Table IV, this ranking is somewhat consistent with the expected ranking based on the Young's moduli reported for the single-crystalline or poly-crystalline forms of these materials, except that single-crystalline Al$_2$O$_3$ has a substantially higher Young's modulus of 450 ± 20 GPa[243,244] (i.e., single-crystal Al$_2$O$_3$ > BeO > AlN > HfO$_2$). As will be discussed later, the substantially reduced mechanical properties for ALD Al$_2$O$_3$ relative to single-crystalline Al$_2$O$_3$ (sapphire) are due to the greatly reduced mass density of ALD Al$_2$O$_3$.

Concerning the Young's modulus and hardness of PEALD AlN, the value of 200 ± 24 GPa is roughly 55% of that reported for single-crystalline 2H-AlN by Yonenaga.[245] This is consistent with the reduced mass density of PEALD AlN relative to that for 2H-AlN (i.e., 2.7 vs. 3.26 g/cm^3) and is supported by recent DFT calculations by Vashishta[143] which have shown that for amorphous AlN, a 10% reduction in density can result in Young's modulus decreasing from ∼375 GPa to <275 GPa. Relative to other forms of AlN, the Young's modulus for amorphous PEALD AlN is also substantially reduced relative to the values of 300–320 GPa reported for poly-crystalline AlN deposited by various sputtering methods,[246–248] but significantly higher than the value of 66 ± 3 GPa reported by Ilic[61] for an ALD grown AlN film. For the latter, we note that Ilic reports a substantially lower mass density of 2.3 ± 0.1 g/cm^3 relative to the value of 2.7 ± 0.1 g/cm^3 determined by NRA-RBS for the PEALD AlN film in this investigation. With respect to the hardness of the PEALD AlN, the value of 22 ± 4 GPa determined in this study is significantly higher than the value of 17 GPa reported for a single-crystal AlN substrate,[245] but consistent with the value of 22 GPa previously reported for a sputter-deposited poly-crystalline AlN thin film.[247]

The nanoindentation Young's modulus of 177 ± 5 GPa for the ALD HfO$_2$ film is also substantially reduced relative to the theoretical value of 300 GPa determined for single-crystalline monoclinic HfO$_2$ in the DFT calculations of Wu,[249] and the value of 283.6 GPa reported by Dole[250] for unstabilized poly-crystalline monoclinic HfO$_2$. However, it is close to the range of 200–250 GPa reported by Wang for dense poly-crystalline HfO$_2$ ceramics of varying purity and microstructure.[144] These observations are consistent with both the ALD HfO$_2$ film exhibiting a nano-crystalline monoclinic structure in XRD and the NRA-RBS mass density being only slightly reduced relative to the theoretical single-crystal density (10.1 g/cm^3)[250] and nearly

Table IV. **Selected Young's modulus (*Y*) and hardness (*H*) values reported for single-crystalline (sc), poly-crystalline (pc), nano-crystalline (nc), and amorphous (a) high-*k* dielectrics in bulk or thin film form on Si.**

Material	Y (GPa)	H (GPa)	Thk. (nm)	ρ (g/cm^3)	Growth (Temperature)	Y Tech.	Ref
pc/sc-BeO	380–420	NR	Bulk	3.0	HP/Sinter	RF	241,242
a/nc-BeO	>330	>33	120	3.0 ± 0.3	RTA (600°C)	NI	TS
a-BeO	330 ± 30	33 ± 5	127	3.0 ± 0.3	ALD	NI	124
sc-AlN	374 ± 10	17 ± 1	Bulk	3.26	HVPE	NI	245
pc-AlN	320 ± 3	NR	Bulk	3.26	HP/Sinter	PE	246
pc-AlN	300	22	1,000	NR	DC-MSpt (RT)	NI	247
a-AlN	200 ± 24	22 ± 4	200	2.7 ± 0.1	PEALD	NI	TS
a-AlN	66 ± 3	NR	21	2.3 ± 0.1	ALD	NMC	61
sc-HfO$_2$	300.5	NR	Bulk	9.9	DFT	DFT	249
pc-HfO$_2$	200–280	NR	Bulk	9.8	HP/Sinter	SR	144,250
a/nc-HfO$_2$	177 ± 5	10 ± 1	200	9.8	ALD (350°C)	NI	TS
a/nc-HfO$_2$	220 ± 40	9.5 ± 2	60	NR	ALD (250°C)	NI	60
a-HfO$_2$	165 ± 13	9.7 ± 0.5	100	NR	ALD (175°C)	NI	251
a/nc-HfO$_2$	166 ± 10	NR	24	9.8	ALD	BLS	253
a-HfO$_2$	152 ± 13	8.4 ± 0.4	150	9.68	RF-Spt (RT)	NI	252
a-HfO$_2$	74 ± 1	NS	21	6.1 ± 0.1	ALD	NMC	61
sc-Al$_2$O$_3$	450 ± 20	NS	Bulk	3.98	CZ/GF	NI	243,244
pc-Al$_2$O$_3$	416 ± 30	15 ± 2	Bulk	3.98	HP/Sinter	NR	254
a-Al$_2$O$_3$	187	11.1	900	3.2	IB (400C)	NI	255
a-Al$_2$O$_3$	197 ± 30	NS	600	3.2 ± 0.3	EBE (400°C)	WC	256
a-Al$_2$O$_3$	220 ± 40	10.5 ± 2	60	NS	ALD (300°C)	NI	60
a-Al$_2$O$_3$	172 ± 8	16 ± 2	200	3.0 ± 0.1	ALD	NI	TS
a-Al$_2$O$_3$	173 ± 11	10 ± 0.6	567	3.1 ± 0.1	ALD (300°C)	NI	64
a-Al$_2$O$_3$	170 ± 5	NS	21	3.1 ± 0.1	ALD	NMC	61
a-Al$_2$O$_3$	180 ± 8	12.3 ± 1	300	NS	ALD (177°C)	NI	42
a-Al$_2$O$_3$	171 ± 1	NS	38	3.1	ALD (120°C)	LAW	257
a-Al$_2$O$_3$	135 ± 7	7.7 ± 0.2	200	NS	ALD (120°C)	NI	65
a-Al$_2$O$_3$	150 ± 2	8 ± 0.3	300	2.7	ALD (100°C)	NI	49
a-Al$_2$O$_3$	125 ± 6	4.8 ± 0.1	150	NS	ALD (80°C)	NI	62
a-Al$_2$O$_3$	117 ± 4	NS	12000	2.3 ± 0.1	RF-Spt (RT)	WC	258

Thk. = thickness, Y. Tech. = Young's modulus measurement technique, NR = not reported, RF = resonant frequency, NI = nanoindentation, PE = pulse echo, NMC = nanomechanical cantilever, DFT = density functional theory, SR = sonic resonance, BLS = Brillouin light scattering, WC = wafer curvature, LAW = laser acoustic wave, HP = hot press, Sinter = powder sintering, RTA = rapid thermal anneal, ALD = atomic layer deposition, HVPE = hydride vapor phase epitaxy, DC-MSpt = DC magnetron sputtering, PEALD = plasma-enhanced ALD, RF-Spt = RF sputtering, Cz = Czochralski crystal pulling, GF = gradient freeze, IB = ion beam deposition, EBE = electron beam evaporation, RT = room temperature, TS = this study.

identical to the densities reported for the dense HfO$_2$ ceramics.[144] Relative to thin-film forms of HfO$_2$, values ranging from as low as 74 GPa to as high as 220 GPa have been reported for ALD and RF-sputter deposited films on Si. Close examination of Table IV, however, shows that this large variation can in part be attributed to differences in deposition temperature, thickness, and mass density. We again note the extremely low value of 74 ± 1 GPa reported by Ilic

Figure 6. Indentation Modulus (*M*) versus indentation depth for the 200 nm ALD HfO$_2$ high-*k* dielectric.

for a 21 nm ALD HfO$_2$ film[61] indicated a mass density of 6.1 ± 0.1 g/cm^3, substantially reduced relative to the values of 9.7–9.8 g/cm^3 reported for the other ALD HfO$_2$ films with considerably higher Young's modulus values.[60,251,252] This may be related to the extremely small thickness for the Ilic HfO$_2$ film relative to the other studies (60–200 nm). Even so, Zizka[253] determined a substantially higher density (9.8 g/cm^3) and modulus (166 ± 10 GPa) for an ALD HfO$_2$ film of similar thickness.

We also note that for the Young's moduli of the remaining HfO$_2$ films listed in Table IV, these values clearly scale with growth/deposition temperature. This observation is consistent with additional measurements performed by Berdova and Venkatachalam on ALD HfO$_2$ films grown at temperatures ≤225°C and then subsequently annealed at temperatures of 700–1000°C.[251,252] For such films, both authors observed a significant increase in both Young's modulus and hardness (10–35%) that they attributed to increased densification and crystallization of the ALD films. Regarding the Young's modulus for the ALD HfO$_2$ film in this study exceeding those reported for other ALD HfO$_2$ films, we note that the higher deposition temperature (>300°C) and larger film thickness could both contribute to increased crystallization of the formed film[180,181] and lead to a Young's modulus more closely approaching that of the theoretical single-crystalline value.

As noted previously, the Young's modulus and hardness for the ALD Al$_2$O$_3$ film investigated in this study is even more substantially reduced (>65%) relative to the values reported for single-crystalline[243,244] and bulk poly-crystalline[254] Al$_2$O$_3$. This is in contrast to the reduction of 35–45% observed for the other high-*k*
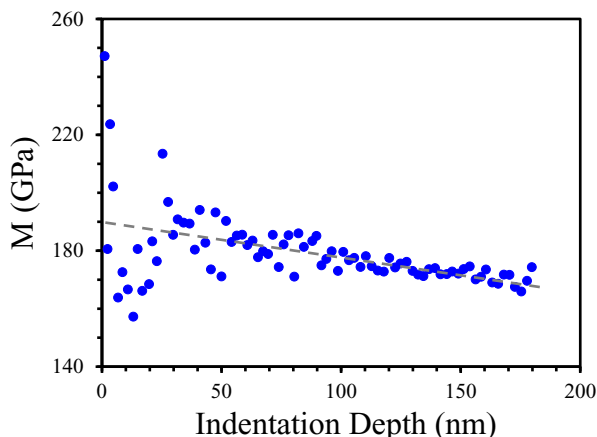
films and can be largely explained by the more significant reduction in the mass density of the ALD Al_2O_3 film (3.0 ± 0.1) relative to the theoretical density of crystalline Al_2O_3 (3.98 g/cm^3).[255] However, the Young's modulus and hardness values of 172 ± 8 and 16 ± 2 GPa, respectively, for the ALD Al_2O_3 film in this study are consistent with the range of values reported for Al_2O_3 films deposited by ALD and other methods (Y = 120–200 GPa, H = 6–15 GPa).[49,61–65,255–259] As for HfO_2, Table IV shows that there is a clear growth temperature dependence for both Young's modulus and hardness with both increasing with increasing growth temperature. This is consistent with more detailed studies by Ylivaara of the dependence of ALD Al_2O_3 mechanical properties on growth temperature where Young's modulus and hardness were observed to increase from 138 ± 8 and 7.9 ± 0.2 GPa, respectively, to 172.8 ± 10.8 and 10.3 ± 0.6 GPa as the growth temperature increased from 100 to 300°C.[64]

Relative to SiO_2, all the high-k films have substantially higher values of Young's modulus and hardness (see Table III). However, relative to SiN:H, the high-k dielectrics exhibit more comparable values, with the PEALD AlN film exhibiting nearly the same value as that for the specific SiN:H film selected for comparison in this study. This is consistent with the fact that single-crystalline and poly-crystalline Si_3N_4 have very comparable Young's modulus values of 330–540[260,261] and 362–312[262,263] GPa, respectively, that depends on both crystal orientation and polytype. We also note that the values of Young's modulus and hardness for PECVD and LPCVD SiN:H have been reported to range from 100–280 GPa and 13–27 GPa, respectively, depending on the exact growth conditions and hydrogen content.[137,264,265] In contrast, the Young's modulus of single crystalline SiO_2 (quartz) is quite low at 95 GPa,[244] and the range of Young's moduli values reported for SiO_2 thin films deposited by a variety of methods is quite small at 60–100 GPa.[266–268]

Film stress.—The high-k dielectric film stress values derived from the pre/post wafer curvature measurements are summarized in Table III. As can be seen, the ALD Al_2O_3 and HfO_2 films both have tensile stresses of 278 and 565 MPa, respectively, while the AlN film at −2.3 GPa is under an extreme state of compression. The film stress for the ALD Al_2O_3 film in this study is slightly lower than some of the previously reported values for 50–100 nm thick films similarly grown using TMA/H_2O, for example, 422 ± 21 MPa reported by Miller,[269] 347–407 MPa reported by Berdova,[63] and 383–474 MPa reported by Tripp.[42] However, more comprehensive studies by Ylivaara[64] have shown that the film stress for ALD Al_2O_3 grown using TMA/H_2O is constant over a thickness of 25–600 nm and decreases from ~525 MPa for growth at 100°C to ~200 MPa as the growth temperature increases to 300°C. This is consistent with the ALD Al_2O_3 films with higher reported tensile stresses being grown at temperatures substantially below the growth temperature used in this study (155–220°C vs. >300°C). We also note that Proost has observed a similar dependence of film stress on growth temperature for electron beam evaporated (EBE) Al_2O_3 films where the tensile stress was observed to decrease from 540 ± 97 MPa for growth at 170°C to 215 ± 15 MPa for growth at 400°C.

For ALD HfO_2, several prior investigations have reported a range of film stress values spanning from 557 MPa for ALD HfO_2 growth at 100°C to 720 MPa for ALD HfO_2 growth at 260 to 420°C.[270,271] Additionally, Shestaeva has reported the film stress for PEALD HfO_2 to range from 611 to 917 MPa depending on the growth temperature.[30] Thus, the value of 565 MPa determined for the ALD HfO_2 film in this study, is on the low end, but still consistent with, the range of values reported in the literature.

For PEALD AlN, we are unaware of any prior film stress measurements. We do note that the compressive stress of the film is consistent with the use of a plasma-activated nitrogen source. Several PECVD studies have shown that significant compressive stresses can be induced due to bombardment of the film by ions created in the plasma and accelerated across the plasma sheath toward the film surface.[272,273] By controlling the plasma potential and drive frequency, the stress in PECVD SiN:H films can be easily tuned from tensile to
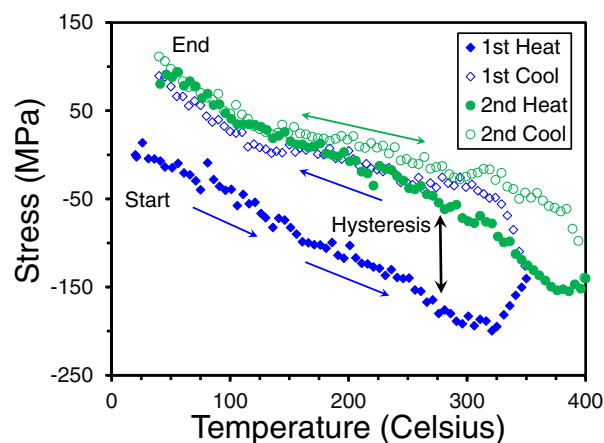

Figure 7. Wafer curvature/film stress vs. temperature for ALD HfO_2 illustrating in-plane CTE measurements.

compressive.[137] It has similarly been shown that energetic ions from the plasma activated step in PEALD processes can also be utilized to induce compressive stresses in what are typically tensile films when grown by pure thermal ALD processes.[274–276]

For the ALD BeO film, we note that the film stress was not measured due to the lack of a wafer curvature measurement instrument in the laboratory housing the BeO ALD system, that is the ALD Al_2O_3, HfO_2, and PEALD AlN growths were performed in separate and geographically remote laboratories.

In-plane CTE.—Representative stress versus temperature curves used to calculate in-plane CTE are shown in Figure 7 for the ALD HfO_2 film. As shown, the wafer curvature/film stress was monitored through two room temperature to 350–400°C heat and cool cycles. For the first heat cycle, some hysteresis was observed with a significant offset of approximately 100 MPa in film stress existing between the heat and cool stages. For the second heat cycle, no hysteretic behavior was observed as evidenced by the heat and cool traces closely following one another. This type of hysteresis has been previously observed in the thermal stress behavior of SiC:H, SiN:H, SiON, SiO_2, and Al_2O_3 thin films annealed under vacuum at temperatures of 300–500°C.[140,258,276–280] In most cases, the hysteretic behavior has been attributed to hydrogen loss and bond rearrangement resulting from heating the films above their deposition temperatures.[276–280] However, we have previously observed such hysteretic behavior from SiC:H films where the deposition temperature was not exceeded during the CTE measurement.[140] For dense SiC:H films such as in this study, no significant hydrogen loss or bond re-arrangement was detected by either FTIR or NRA-RBS, implying that the observed hysteretic behavior is due instead to strained bond relaxation. As the deposition temperatures for the ALD films investigated in this study were not exceeded, we attribute the observed hysteretic behavior for these films to strained bond relaxation as well.

Using the slope of the second heat/cool cycle in Fig. 7, the in-plane CTE for HfO_2 was determined to be 4.4 ppm/°C assuming isotropic thermal and mechanical properties. The validity of this latter assumption will be discussed after presentation of the out-of-plane CTE measurements in the next section. However, we do note that this value is consistent with the range of 4–6 ppm/°C determined using similar methods by Gulch for pure ALD HfO_2 films as presented in Table V.[270] It is also consistent with the range of 4.4–6.5 ppm/°C reported by Wang for poly-crystalline HfO_2 bulk ceramics.[144]

Similar wafer curvature versus temperature measurements performed with the ALD Al_2O_3 film led to the determination of an in-plane CTE value of 3.8 ppm/°C, again assuming isotropic properties. This value is slightly lower but in close agreement with

Table V. Selected coefficient of thermal expansion (CTE) values reported for single-crystalline (sc), poly-crystalline (pc), nano-crystalline (nc), and amorphous (a) high-*k* dielectrics.

Material	IP / c‖ CTE (ppm/°C)	OOP / c⊥ CTE (ppm/°C)	Method	Density (g/cm^3)	Ref.
sc-BeO (bulk)	5.35 (c‖)	5.99 (c⊥)	XRD	3.01	291
nc-BeO (film)	–	6.0 ± 1.1 (OOP)	XRR	3.0 ± 0.3	TS
sc-AlN (bulk)	3.48 (c‖)	4.35 (c⊥)	XRD	3.26	291
sc-AlN (bulk)	4.2 (c‖)	5.3 (c⊥)	XRD	NS	283
pc-AlN (bulk)	4.4–4.8	–	DMA	NS	285
pc-HfO$_2$ (bulk)	7.5 (c‖)	3.7 (a‖) 0.8 (b‖)	NS	NS	292
pc-HfO$_2$ (bulk)	4.4–6.5	–	NS	NS	144
a-HfO$_2$ (film)	4–6 (IP)	–	WC	NS	270
a/nc-HfO$_2$ (film)	4.4 (IP)	2.4 ± 0.2 (OOP)	WC/XRR	9.8 ± 0.3	TS
sc-α-Al$_2$O$_3$ (bulk)	4.4 (c‖)	3.3 (c⊥)	XRD	3.986	283
sc-α-Al$_2$O$_3$ (bulk)	7.7 (c‖)	–	WC	3.986	284
sc-α-Al$_2$O$_3$ (bulk)	5.74 (c‖)	5.1 (c⊥)	LHS	3.986	281
sc-κ-Al$_2$O$_3$ (bulk)	5.1 (c‖)	3.8 (c⊥)	XRD	NS	282
pc-Al$_2$O$_3$ (bulk)	4.6	–	NS	3.984	254
a-Al$_2$O$_3$ (film)	4.2 (IP)	–	WC	3.0	269
a-Al$_2$O$_3$ (film)	5.2 ± 0.3 (IP)	–	WC	3.2 ± 0.3	256
a-Al$_2$O$_3$ (film)	7.1 ± 0.3 (IP)	–	WC	2.3	258
a-Al$_2$O$_3$ (film)	3.8 (IP)	2.1 ± 0.2 (OOP)	WC/XRR	3.0 ± 0.1	TS

c‖ = parallel to c-axis, c⊥ = perpendicular to c-axis, ppm = part per million, IP = in-plane, OOP = out-of-plane, XRD = X-ray diffraction, XRR = X-ray reflectivity, DMA = dynamic mechanical analysis, WC = wafer curvature, LHS = longitudinal expansion, NS = not specified, TS = this study.

the value of 4.2 ppm/°C determined by Miller via similar wafer curvature–temperature measurements performed on a 100 nm ALD Al$_2$O$_3$ film grown at 275°C using TMA and H$_2$O.[269] Both values are also in reasonable agreement with the values of 5.0 ± 0.1 and 5.3 ± 0.2 ppm/°C determined by Proost for EBE Al$_2$O$_3$ films grown at temperatures of 200 and 400°C, respectively.[256] All these values compare well to those reported for single-crystalline and poly-crystalline Al$_2$O$_3$ ceramics. Specifically, Yates has reported a room temperature CTE of 5.1–5.7 ppm/°C for single-crystal α-Al$_2$O$_3$,[281] Halvarrson has reported a CTE of 3.8–5.1 ppm/°C for single-crystal κ-Al$_2$O$_3$,[282] and Munro has reported a room temperature CTE of 4.6 ppm/°C for poly-crystalline Al$_2$O$_3$ ceramics.[254] We do note that a slightly higher value of 7.1 ± 0.3 has been reported by Thurn for a room temperature sputter deposited Al$_2$O$_3$ film with a substantially lower density of 2.3 g/cm^3 and Young's modulus of 117 ± 4 GPa.[258] Also, Yim[283] and Retajcyzk[284] both report CTE values of 7.3–8.1 for various orientations of sapphire (α-Al$_2$O$_3$). For the latter, we note the temperature-dependent CTE data of both Yates and Halvarsson show that the CTE for α-Al$_2$O$_3$ increases to ∼7 ppm/°C at 400°C, indicating that part of the discrepancy may be due to differences in the quoted or measured temperature range.

In-plane CTE measurements for the PEALD AlN film were unsuccessful due to the high compressive stress in the film resulting in the wafer curvature being beyond the detection limits of the FSM instrument. We are unaware of any other CTE measurements of AlN thin films. However, we do note for reference that Yim has reported the CTE for single-crystalline wurtzite AlN to be 5.3 and 4.2 ppm/°C for expansion perpendicular and parallel to the *c*-axis, respectively.[283] Boey has also reported a CTE of 4.4–4.8 ppm/°C for porous poly-crystalline AlN ceramics.[285] Regarding the ALD BeO film, in-plane CTE measurements were not performed due to the film being deposited on a substrate smaller than the wafer requirements of the FSM instrument. Instead, out-of-plane CTE measurements were performed on the ALD BeO film, which will be described in the following section.

Both of the in-plane CTE values determined for the ALD HfO$_2$ and Al$_2$O$_3$ films are comparable to those obtained for other amorphous thin films. As shown in Table VI, there have been several investigations of the in-plane CTE for both a-SiN:H and SiO$_2$ thin films deposited by various methods with reported values of 1.5–4 and 0.5–2 ppm/°C, respectively.[278,279,284–290] For the specific a-SiN:H film included in this investigation for comparison, an in-plane CTE of 1.2 ± 0.3 ppm/°C

was determined (see Table III), which is on the low end of the distribution of in-plane CTE values reported for similar or related PECVD and LPCVD SiN films (see Table VI). For the thermal oxide, the CTE was below the resolution of the FSM instrument (∼1 ppm/°C) which is consistent with the very low values of 0.5–0.6 ppm/°C reported by Sinha and Blech.[287,290]

Out-of-plane CTE.—Representative X-ray reflectivity data used to determine the out-of-plane CTE for the ALD BeO film are shown in Figure 8. As the dielectric thin films are heated, the Kiessig fringes shift to a lower angle, indicating a thicker film. The reflected intensity as a function of angle is modeled,[145] which accurately yields film thickness at each of the temperatures used, as shown in Figure 9. The change in thickness as a function of temperature can then be used to determine the CTE. The out-of-plane CTEs of BeO, Al$_2$O$_3$, and HfO$_2$ films were accordingly determined to be 6.0 ± 0.1, 2.1 ± 0.2, and 2.4 ± 0.2 ppm/°C, respectively. The intermediate data also indicate that over the temperature range shown, a linear increase in out-of-plane thickness with temperature is a good model. Below 200°C, the BeO films did not exhibit a linear trend, hence the limited range of data shown here. Future experiments are necessary to determine whether this is due to an experimental or material factor. The residual compressive strain in the AlN thin films resulted in delamination of the film when heated to 300°C, below the deposition temperature of 350°C. At 200°C, the films were still intact, but over this narrower temperature range the change in thickness of the AlN layer could not be reliably determined by the reflectivity technique due to a rough surface and presumed low CTE.

For the ALD BeO film, we note that the out-of-plane CTE of 6.0 ppm/°C is in excellent agreement with the room temperature CTE of 5.4–6.0 ppm/°C reported for the various crystal directions of single crystal wurtzite BeO by Iwanaga.[291] Interestingly, the out-of-plane CTE for ALD Al$_2$O$_3$ and HfO$_2$ of 2.1 and 2.4 ppm/°C, respectively, are both significantly lower than the in-plane CTE values of 3.8 and 4.4 ppm/°C, respectively. This is in contrast to prior measurements performed on PECVD a-SiC:H where a general agreement between in-plane and out-of-plane CTE was found,[140] and thus confirmed the assumption of isotropic material properties in that study. The observations of different in-plane and out-of-plane CTE values for Al$_2$O$_3$ and HfO$_2$ therefore suggests these two materials possess some anisotropy in CTE, and calls into question the general assumption of isotropy for other material properties.

Table VI. Selected coefficient of thermal expansion (CTE) values reported for various silicon-based amorphous dielectrics.

Film (Method)	In-plane CTE (ppm/°C)	E (GPa)	CTE Method	Density (g/cm^3)	Ref
SiN:H (PECVD)	2.7–4.0	86–130	WC	1.8–2.5 (N/Si = 1.3)	273
SiN:H (LPCVD)	1.6	370	WC	NS	284
SiN:H (PECVD)	1.5	110	WC	NS	284
SiN:H (PECVD)	1.8–2.7	90–150	WC	NS	286
SiN:H (PECVD)	2.4	340	WC	NS	287
SiN:H (PECVD)	1.4–3.4	133–214	WC	NS	278
SiN (PECVD)	4.7	73 ± 3	WC	NS	279
SiN (PECVD)	2.8 ± 0.1	138–386	WC	2.6–3.0 (N/Si = 1 – 1.5)	264
SiN:H (LPCVD)	2.2 ± 0.2	260–360	WC	NS	288
SiN:H (LPCVD)	1.6	370	WC	NS	284
SiN (CVD)	2.8 ± 0.1	344	WC	3.0 (N/Si = 1.33)	264
SiON (PECVD)	2.2–4.8	39–51	WC	NS	279
SiO$_2$ (PECVD)	2.1 ± 0.3	41–44	WC	NS	279
SiO$_2$ (PECVD)	2.2–2.6	40–43	WC	2.0	289
SiO$_2$ (FQ)	0.5	90	WC	NS	284
SiO$_2$ (Thermal)	0.6	160	WC	NS	287
SiO$_2$ (Thermal)	0.5	46–51	WC	NS	290
a-Si:H (PECVD)	4.4	150	WC	2.0 (20%H)	289

CVD = chemical vapor deposition, PECVD = plasma-enhanced CVD, LPCVD = low-pressure CVD, WC = wafer curvature, Thermal = thermal oxidation, FQ = fused quartz, NS = not specified.

Given the observed nano-crystalline monoclinic structure for the ALD HfO$_2$ film, some anisotropic behavior is perhaps not unexpected. Recent high temperature X-ray diffraction measurements by Haggerty have shown a substantial degree of anisotropy for the CTE of monoclinic HfO$_2$ with values of 3.7, 0.8, and 7.5 ppm/°C being reported for room temperature thermal expansion along the *a*, *b*, and *c* axis, respectively (see Table V).[292] In this regard, the in-plane CTE of 4.4 ppm/°C is in excellent agreement with both the mean of these three values as well as the mean in-plane CTE expected of a film with [001] texture, while the low out-of-plane CTE of 2.4 ppm/°C suggests possible *a*- or *b*-axis orientation for the nano-crystallites in the HfO$_2$ film. This is consistent with the observations of Ritala where crystallites with a preferential orientation in the [100] direction was observed for ALD HfO$_2$ films.[181] However, we note that a more random orientation has been reported by others for thinner films[56,60] and a [111] orientation has been reported by Berdova for ALD HfO$_2$ films annealed at 700–900°C.[251] Thus, while the measured CTE values can be reasonably explained by literature precedent, the grain orientation (or lack of orientation) in ALD HfO$_2$ films is likely highly dependent on the film thickness and specific growth conditions.

This of course neglects the possible presence of anisotropy in the Young's modulus of the ALD HfO$_2$ film. We do note that recent Brillouin light scattering measurements by Zizka[253] on a 25 nm ALD HfO$_2$ film have confirmed isotropic mechanical properties. As previously discussed, this is consistent with ALD HfO$_2$ initially growing amorphous and starting to become increasingly crystalline at thicknesses >25 nm.[180,181] For the 200 nm ALD HfO$_2$ film in this study, XRD did show the presence of some crystallinity, and hence some anisotropy in *Y* and *H* could be expected. Unfortunately, we do not currently have the ability to independently determine the in-plane and out-of-plane modulus for thin films of this type. However, based on the elastic constants published by Wu for single-crystalline monoclinic HfO$_2$,[249] the anisotropy in Young's modulus between the primary crystallographic directions could be as high as 45–55%. This is roughly the difference observed here between in-plane and out-of-plane CTE.
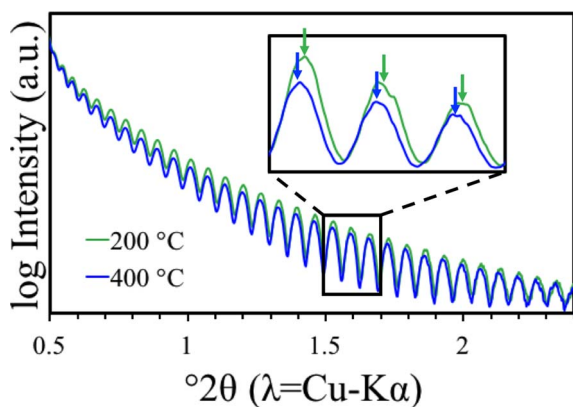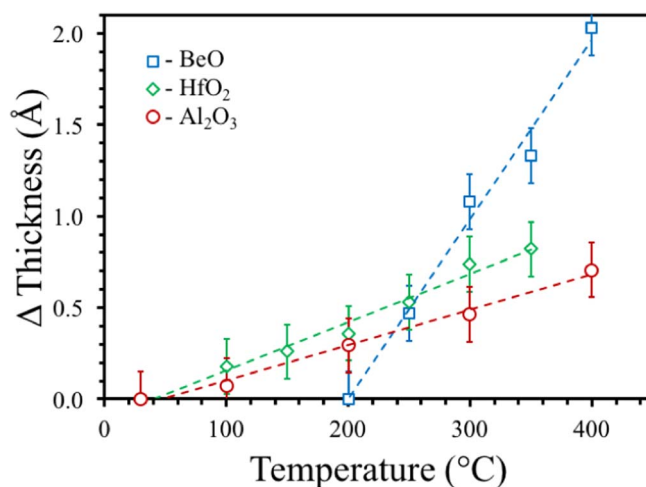
Figure 8. Reflectivity data for the ALD BeO film at two different temperatures. The systematic shift of peaks to lower angle in the 400°C scan indicate a slightly thicker film relative to the scan at 200°C. For clarity only a portion of the angular range is shown.

Figure 9. Change in thickness for ALD BeO, Al$_2$O$_3$, and HfO$_2$ films measured by XRR as a function of temperature. The reference thicknesses taken at 200°C for BeO and 30°C for Al$_2$O$_3$ and HfO$_2$ are 1282.39 Å, 1022.75 Å, and 1183.35 Å, respectively. Error bars are 0.15 Å, as given by the standard deviation between multiple thickness measurements as discussed in the Experimental section.

For single-crystal Al$_2$O$_3$, Yim and Yates have reported similar anisotropies in CTE with values of 4.4–5.7 for expansion parallel to the *c*-axis and 3.3–5.1 for expansion perpendicular to the *c*-axis.[281,283] The values measured here are lower, with CTE values of 3.8 ppm/°C parallel and 2.1 ppm/°C perpendicular to the substrate. This is perhaps due to the elevated oxygen content in the films (~1:2 Al:O). The degree of anisotropy previously measured in crystalline Al$_2$O$_3$ is consistent with the differences observed in our in-plane and out-of-plane CTE measurements for ALD Al$_2$O$_3$. However, the Al$_2$O$_3$ film in this study was found to be X-ray amorphous and hence the observation of anisotropy is more puzzling. One possible explanation could be the presence of some degree of undetected crystallinity. This seems unlikely given the extremely high temperatures needed to crystallize ALD Al$_2$O$_3$ films.[182,183] Another possible explanation could be a simple calibration offset or difference in the lower detection limit for CTE between the two techniques. The former seems unlikely given prior measurements on a-SiC:H have shown excellent agreement between in-plane and out-of-plane CTE measurements,[140] and reasonable agreement was also observed in this study for the comparison PECVD a-SiN:H film where isotropic mechanical properties have been well established by multiple authors (see Table III).[145,293,294] The latter seems unlikely as the lower limit for our in-plane CTE measurement is ~1 ppm/°C, which is well below the out-of-plane CTE value of 2.1 ± 0.2 ppm/°C for ALD Al$_2$O$_3$. One final possibility is related to the thermal stability of ALD Al$_2$O$_3$ and differences in the thermal history associated with each CTE measurement. As shown in Fig. 7, hysteretic behavior is observed in the first heat/cool cycle for the in-plane CTE/wafer curvature measurement implying some initial thermal instability. For the out-of-plane CTE measurements, some slight (<0.1%) film shrinkage is observed in the initial heat/cool cycles and multiple heat/cool cycles are typically required to stabilize the film.[140] Thus, the differences in in-plane and out-of-plane CTE may be related to the different thermal histories associated with each measurement.

Thermal conductivity.—Figure 10 presents an exemplary TDTR temporal cooling curve for the ALD Al$_2$O$_3$ high-*k* film. Each data point is the average of four scans at spatially different locations on the sample. The solid red line through the data is representative of the quality of fit to the thermal model for each of the samples tested in this study, even though for Fig. 10 it is specific to the Al$_2$O$_3$ sample. This quality of fit to the data and the inset figure showing a sensitivity plot for this measurement reinforces that the thermal model is most
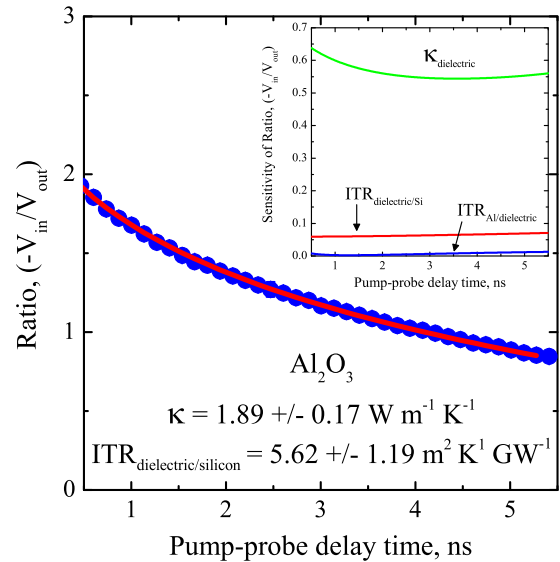

Figure 10. Averaged data from four tests on the ALD Al$_2$O$_3$/silicon sample. The fit to the data (solid red line) and standard deviation from tests are smaller than the data points. The error reported on the best fit values for κ and ITR are largely due to uncertainty in the thickness of the metal transducer and not from test to test repeatability. The inset plotting sensitivity for the ALD Al$_2$O$_3$ sample shows maximum sensitivity to thermal conductivity of the high-*k* dielectric layer over the interfaces on either side of the dielectric.

sensitive to uncertainty in the thickness of the metal transducer and the cross-plane thermal conductivity of the dielectric film and show that the test-to-test variation is negligible. The thickness of the aluminum transducer is characterized by both mechanical profilometry and picosecond acoustics and is determined to be 80 ± 3 nm. With the uncertainty of the thickness of the aluminum transducer accounted for in the error of the measurement, we are able to isolate the thermal conductivity of the dielectric layer as the most sensitive parameter, more so than the interface resistances on either side of that layer, ITR$_{Al/dielec}$ and ITR$_{dielec/Si}$, as shown in the inset of Fig. 10. While Fig. 10 also shows that we are less sensitive to the resistance between the dielectric and the silicon than the thermal conductivity of the dielectric, the sensitivity in this particular measurement allows us to fit both

Table VII. Summary of previously reported values of interfacial thermal resistance between BeO, AlN, Al$_2$O$_3$, and HfO$_2$ films and silicon substrates.

Film	ITR (m² K GW⁻¹)	Thickness (μm)	Density (g/cm³)	Bulk/Film (Growth Method)	Meas. Method	Ref. #
nc/a-BeO	11.8 ± 0.2	0.128	3.0 ± 0.3	Film (ALD)	TDTR	TS
nc/BeO	11.7 ± 0.6	0.128	3.0 ± 0.3	Film (ALD)	TDTR	TS
pc-AlN	3.5–36	0.1 − 4	NS	Film (MS)	UTHS	311
pc-AlN	65–85	0.1 − 4	3.3	Film (MS)	PTR	310
pc-AlN	10–25	0.15 − 3.5	NS	Film (MS)	UTHS	173
a-AlN	39.5 ± 5.3	0.2	2.7 ± 0.1	Film (PEALD)	TDTR	TS
a-Al$_2$O$_3$	5.81 ± 1.5	0.1	3.0 ± 0.1	Film (ALD)	TDTR	TS
a/nc-HfO$_2$	3.0 − 13	0.005 − 0.02	NS	Film (ALD)	TDTR	56
a/nc-HfO$_2$	28 ± 3.4	0.128	9.8 ± 0.2	Film (ALD)	TDTR	TS
SiO$_2$	14.5 ± 1.4	0.18	2.2 ± 0.1	Film (Thermal)	TDTR	TS
a-SiN:H	10 ± 0.7	0.1–0.5	2.8	Film (PECVD)	TDTR	TS

Note: NS = Not specified, NA = Not applicable, ALD = Atomic layer deposition, MS = Magnetron Sputtering, PEALD = Plasma enhanced ALD, Thermal = Thermal Oxidation, PECVD = Plasma Enhanced CVD, TDTR = Time domain thermoreflectance, UTHS = Ultrafast transient hot strip, PR = Photothermal Reflectance, TS = This study.

Table VIII. Summary of previously reported values of thermal conductivity for BeO, AlN, Al$_2$O$_3$, and HfO$_2$.

Film	κ (W/mK)	Thickness (μm)	Density (g/cm^3)	Bulk/Film (Growth Method)	Meas. Method	Ref. #
c-BeO	370	NA	3.0	Bulk	LHS	306
pc-BeO	260–320	NA	3.0	Bulk	NS	307
pc-BeO	260 (parr.) 60 (perp.)	1.6	3.0	Film (R-ICB)	NS	192
nc/a-BeO	15.6 ± 3	0.2	3.0 ± 0.3	Film (ALD)	TDTR	TS
c-AlN	320	NA	3.21	Bulk	LHS	308
pc-AlN	2–210	0.1–2.5	NS	Film (MS)	UTHS, 3ω, TDTR,	310–314
nc-AlN	1.0	0.3	NS	Film (PLD)	3ω	309
a-AlN	1.7 ± 0.5	0.1	3.3	Film (MS)	TDTR	310
a-AlN:H	3 ± 0.3	0.2	2.7 ± 0.1	Film (PEALD)	TDTR	TS
c-Al$_2$O$_3$	34	NA	3.98	Bulk	LFA, 3ω	317,318
pc-Al$_2$O$_3$	16–20	NA	3.9	Bulk	LFA	320
a-Al$_2$O$_3$	1.1–1.8	0.5–2	3.4 ± 0.1	Film (MS)	3ω	324
a-Al$_2$O$_3$	0.7–1.1	0.2–1.7	3.98	Film (EBE)	TP, TC	326,327
a-Al$_2$O$_3$	1.6 ± 0.2	0.14	NS	Film (AO)	FM	321
a-Al$_2$O$_3$	1.3–2.6	0.01–0.1	2.7–3.1	Film (ALD)	TDTR, Raman	57–59
a-Al$_2$O$_3$	2.1 ± 0.2	0.2		Film (ALD)	TDTR	TS
pc-HfO$_2$	1.5–2.0	NA	9–9.5	Bulk	LFA	322
nc-HfO$_2$	1.2–2.5	0.09–2	9.1	Film (MS)	TDTR, 3ω	323,324
a/nc-HfO$_2$	0.5–1.7	0.005–0.1	NS	Film (ALD)	TDTR, 3ω	56,57
a-HfO$_2$	0.3 ± 0.1	0.003	NS	Film (MBE)	STM	325
a-HfO$_2$	≤ 0.05	0.15–2	9.68	Film (EBE)	TP,TC	326,327
a/nc-HfO$_2$	4.1 ± 0.6	0.2	9.8 ± 0.2	Film (ALD)	TDTR	TS

Note: NS = Not specified, NA = Not applicable, R-ICB = Reactive ionized-cluster beam, ALD = Atomic layer deposition, MS = Magnetron Sputtering, PLD = Pulsed laser deposition, PEALD = Plasma enhanced ALD, EBE = Ebeam evaporation, AO = Anodic oxidation, MBE = Molecular beam epitaxy, LHS = Longitudinal heat flow, TDTR = Time domain thermoreflectance, UTHS = Ultrafast transient hot strip, 3ω = 3 Omega, LFA = Laser flash analysis, TP = Thermal pulse, TC = Thermal comparator, FM = Free membrane, Raman = Raman Spectroscopy, STM = Scanning thermal microscopy, TS = This study.

the thermal conductivity and the interface resistance with our thermal model. Table VII summarizes the ITR values from this study along with those from prior studies of similar materials. Table VIII similarly summarizes the thermal conductivities determined by TDTR in this study along with those from other studies on related materials.

The previous literature available for the ITR between dielectrics and silicon are relatively sparse. In the case of Al$_2$O$_3$ and BeO, to our knowledge, these are the first measurements of boundary conductance across these specific interfaces. Furthermore, the HfO$_2$ results presented by Panzer offer the only other literature values for ITR at ALD deposited dielectric/silicon interfaces.[56] The values obtained for the interfaces in the previous work in the literature are dependent on the method used, assumptions made in the thermal model and property extraction, specimen quality, as well as the quality of the interface between the two materials. In this regard, the data presented here offer a consistent comparison of the interface between six dielectric materials, including the SiO$_2$ and a-SiN:H, with which to evaluate the relative difference in ITR for ALD dielectrics on the same substrate using the same procedure and testing method for ITR extraction.

Figure 11 summarizes and compares the measured thermal conductivities versus dielectric constant for the high-*k* dielectrics in addition to thermal SiO$_2$ and PECVD SiN:H. As can be seen, the high-*k* dielectrics all have higher thermal conductivities relative to measured values of 1.5 ± 0.1 and 1.7 ± 0.2 W/mK for thermal SiO$_2$ Refs. 295–299 and PECVD SiN:H, Refs. 300–304 respectively. Amongst the high-*k* dielectrics, BeO clearly has the highest thermal conductivity at >15 W/mK. This is consistent with single crystalline BeO having the highest reported thermal conductivity for all known dielectric ceramics.[305] However, the value measured here for ALD BeO is substantially less than the value of 370 W/mK reported by Slack for bulk single-crystalline BeO[306] and the range of values (220–320 W/mK) reported for bulk poly-crystalline BeO ceramics.[307] For BeO thin films, we are aware of only a single prior investigation by Takagi where the thermal conductivity for highly (0001) *c*-axis oriented poly-crystalline wurtzite BeO thin films deposited by a reactive ionized cluster beam method at 400°C on glass substrates was reported.[192] For heat flow par-

allel to the (0001) *c*-axis of the grains, Takagi reported a high thermal conductivity of 260 W/mK. However, the thermal conductivity perpendicular to the grains was found to be greatly reduced at 60 W/mK. This indicates that while XRD for the ALD BeO film showed the presence of some crystallinity, the film is likely poly/nano-crystalline with no preferential grain orientation. The presence of unoriented grain boundaries probably creates additional phonon scattering that reduces the effective thermal conductivity of the film below that observed by Takagi.[192] It is also possible that the ALD BeO film contains some amorphous regions with a lower effective thermal conductivity that can also act as additional scattering centers to further reduce the phonon mean free path. Additionally, the presence of the boundary between the dielectric and silicon offers yet another scattering mechanism.
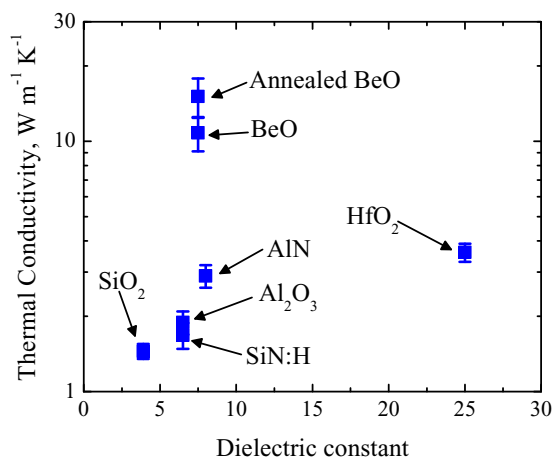

Figure 11. Thermal conductivity vs. dielectric constant for high-*k* dielectrics investigated in this study plus representative values for thermally grown SiO$_2$ and PECVD SiN:H.[295–304]

While there have been relatively few prior investigations of the thermal conductivity for BeO thin films, there have been several prior investigations of amorphous and poly-crystalline AlN, Al_2O_3, and HfO_2 thin films deposited by various methods. The thermal conductivities reported in these studies are summarized in Table VIII along with the deposition method, film thickness(es), mass density, film microstructure (nano-crystalline or amorphous), and thermal conductivity measurement method. For additional comparison, the reported bulk single- and poly-crystalline values for AlN, Al_2O_3, and HfO_2 are also included. Focusing first on AlN, one can see that the span of reported thermal conductivity is quite wide with values as high as 320 W/mK being reported for bulk single-crystal AlN[308] and values as low as 1 and 1.7 W/mK being reported for nano-crystalline[309] and amorphous[310] AlN, respectively. For poly-crystalline AlN films deposited primarily by reactive magnetron sputtering, an equally wide range has been reported of 2–210 W/mK where the variation has been strongly correlated to the crystalline quality and grain orientation.[173,310–314] Interestingly, unbalanced sputtering was found to produce highly crystalline wurtzite AlN films with a strong preferential (0001) c-axis orientation and out of plane thermal conductivities approaching 210 W/mK.[173,310] Balanced sputtering produced AlN films with poorer crystalline quality and greatly reduced values of thermal conductivity.

For amorphous AlN, we are aware only of the study reported by Zhao where the thermal conductivity of 1.7 ± 0.5 W/mK was reported for a 100 nm thick film deposited by magnetron sputtering.[310] This value is reduced but almost within the error bar of the value of 3 ± 0.3 W/mK determined for the PEALD AlN film in this study. We do note that the value of 3 ± 0.3 W/mK is well within the lower bound of values reported for low-crystalline-quality magnetron sputtered AlN.[310–314] The slightly higher value observed in this study could be evidence of some level of crystallinity undetected by XRD or due to enhanced mid-range order. The reduction in the values reported by Zhao could also be due to similar considerations mentioned for the BeO film (i.e., boundary scattering) as the film in this study is 200 nm thick and, as a result, is less sensitive to the underlying boundary. The existence of long wavelength heat carriers has recently been experimentally observed in amorphous silicon films and suggests the nature of energy transport in amorphous films may not be as simple as is often assumed.[315] As the value of 1 W/mK reported by Jacquot for nano-crystalline AlN indicates,[309] the thermal conductivity of AlN may also be a strong function of crystallinity/microstructure.

As noted previously, Duquenne has observed a correlation between the FWHM of the Al−N stretching mode in FTIR to thermal conductivity for sputter deposited AlN films.[173] In this regard, the FWHM for the PEALD AlN film in this study is $\sim$100 cm^{-1}. Sputter deposited AlN films with similar FWHM were found to exhibit poor to very poor crystallinity and bulk thermal conductivities of 2.6–22 W/mK.[173] Thus, our results are again consistent with the lower bounds observed for sputter deposited AlN. We also note that reductions in AlN thermal conductivity have been attributed to the presence of oxygen contamination.[310,311,316] For the PEALD AlN films investigated in this study, the oxygen content was below the detection limits of RBS. Thus, the higher purity of the PEALD AlN film may contribute to the slighly higher measured thermal conductivity despite the observed lack of crystallinity.

Compared to BeO and AlN, single crystal Al_2O_3 (sapphire) exhibits a low thermal conductivity of only 34 W/mK,[317,318] but comparable to the value of $\sim$14 W/mK for single crystal SiO_2 (quartz).[319] The reported thermal conductivities for poly-crystalline[254,320] and amorphous[57–59,321] Al_2O_3 of 16–33 and 0.7–2.6 W/mK, respectively, are also comparable to the previously discussed lower range reported for AlN and amorphous SiO_2 (see Table VIII), indicating that the thermal conductivity for Al_2O_3 is not as sensitive to microstructure as AlN and BeO. Regarding the amorphous ALD Al_2O_3 film investigated in this study, the measured value of 2.1 ± 0.2 W/mK is in excellent agreement with several other recent investigations of the thermal conductivity of ALD Al_2O_3 employing either identical or different measurement techinques.[57–59] Collectively, the results for

ALD Al_2O_3 are also consistent with those for amorphous Al_2O_3 films deposited by other methods.[321]

Regarding HfO_2, we are unaware of any reports of thermal conductivity for single-crystal hafnia. Investigations of bulk ceramic or sputter deposited thin film poly-crystalline hafnia doped/stabilized with yttria for thermal barrier coating applications have reported relatively low thermal conductivities of 1.5–2.0 W/mK.[322,323] Slightly higher values of 1.2–2.5 W/mK have been reported for pure nano-crystalline sputter deposited HfO_2 films.[323,324] However, substantially reduced values of 0.5–1.7 W/mK have been reported for ALD HfO_2 gate oxide films which exhibit a mixed amorphous/nano-crystalline microstructure.[57,324] Purely amorphous films deposited by molecular beam epitaxy[325] or electron beam evaporation[326,327] exhibit still lower thermal conductivity values of 0.3 and <0.05 W/mK, respectively. In this regard, the value of 4.1 ± 0.6 W/mK observed here for an ALD HfO_2 is remarkable and perhaps the highest value reported to date for HfO_2. The increased value observed here could be attributed to the higher mass density and increased degree of crystallinity achieved by growing to substantially higher thicknesses. The propensity for ALD HfO_2 to crystallize as the thickness increases is again well known in the literature.[180,181]

Conclusions

Exhaustive measurements, review, and discussion of the thermal, mechanical, electrical, optical, and structural properties of ALD high-k materials beryllium oxide, aluminum nitride, aluminum oxide, and hafnium oxide have been presented and compared to identical measurements on conventional silicon based dielectrics silicon dioxide and silicon nitride. The results of this full spectrum characterization have shown that, in addition to exhibiting high values of dielectric permittivity and electrical resistance, the ALD high-k materials exhibit equally exceptional thermal and mechanical properties that meet or exceed those of thermally grown SiO_2 and PECVD SiN:H. ALD BeO in particular exhibits extreme values of Young's modulus (>300 GPa) and thermal conductivity ($\geq$15 W/mK) that should make it attractive for some high performance applications. In many cases, the observed extreme thermal and mechanical properties exhibited by the ALD high-k films were found to correlate with the presence of crystallinity despite the relatively low growth temperatures employed. In contrast, some of the electrical and optical properties were found to correlate more strongly with the percentage of ionic vs. covalent bond character in the high-k film. Over all, the ALD high-k dielectrics investigated exhibit both compelling thermal/mechanical and electrical/optical properties.

References

1. S. King, H. Simka, D. Herr, H. Akinaga, and M. Garner, *APL Mater*, **1**, 040701 (2013).
2. G. Wilk, R. Wallace, and J. Anthony, *J. Appl. Phys.*, **89**, 5243 (2001).
3. M. Houssa, L. Pantisano, L.-A. Ragnarsson, R. Degraeve, T. Schram, G. Pourtois, S. De Gendt, G. Groeseneken, and M. M. Heyns, *Mat. Sci. Engr. R*, **51**, 37 (2006).
4. J. Robertson, *Rep. Prog. Phys.*, **69**, 327 (2006).
5. W. Tsai, N. Goel, S. Koveshnikov, P. Majhi, and W. Wang, *Microelectron. Eng.*, **86**, 1540 (2009).
6. G. He, X. Chen, and Z. Sun, *Surf. Sci. Rep.*, **68**, 68 (2013).
7. R. D. Clark, *Materials*, **7**, 2913 (2014).
8. J. Robertson and R. Wallace, *Mat. Sci. Engr. R*, **88**, 1 (2015).

9. F. Pan, S. Gao, C. Chen, C. Song, and F. Zeng, *Mat. Sci. Engr. R*, **83**, 1 (2014).
10. S. Clima, K. Sankaran, Y. Chen, A. Fantini, U. Celano, A. Belmonte, L. Zhang, L. Goux, B. Govoreanu, R. Degraeve, D. Wouters, M. Jurczak, W. Vandervorst, S. De Gendt, and G. Pourtois, *Phys. Stat. Solidi RRL*, **8**, 501 (2014).
11. C. Liu, M. Ostling, and J. Hannon, *MRS Bulletin*, **39**, 658 (2014).
12. A. D. Sheikh and V. L. Mathe, *J. Phys. Chem. Sol.*, **72**, 1423 (2011).
13. J. Hu, T. Nan, N. Sun, and L. Chen, *MRS Bulletin*, **40**, 728 (2015).
14. L. Haspert, S. Lee, and G. Rubloff, *ACS Nano*, **6**, 3528 (2012).
15. J. Klootwijk, K. Jinesh, and F. Roozeboom, *Microelectron. Eng.*, **88**, 1507 (2011).
16. B. Lee, S. Li, G. Von Gastrow, M. Yli-Koski, H. Savin, V. Malinen, J. Skarp, S. Choi, and H. Branz, *Thin Solid Films*, **550**, 541 (2014).
17. J. A. van Delft, D. Garcia-Alonso, and W. M. M. Kessels, *Semicond. Sci. Technol.*, **27**, 074002 (2012).
18. S. Gieraltowska, L Wachnicki, B. Witkowski, R. Mroczynski, P. Dluzewski, and M. Godlewski, *Thin Solid Films*, **577**, 97 (2015).
19. S. Pan, S. Ding, Y. Huang, Y. Huang, D. Zhang, L. Wang, and R. Liu, *J. Appl. Phys.*, **102**, 073706 (2007).
20. G. Ruhl, W. Lehnert, M. Lukosius, C. Wenger, C. Kaynak, T. Blomberg, S. Haukka, P. Baumann, W. Besling, A. Roest, B. Riou, S. Lhostis, A. Halimaou, F. Roozeboom, E. Langereis, W. Kessels, A. Zauner, and S. Rushworth, *ECS J. Solid State Sci. Technol.*, **3** N120 (2014).
21. T. Cook Jr., C. Fulton, W. Mecouch, R. Davis, G. Lucovsky, and R. Nemanich, *J. Appl. Phys.*, **94**, 7155 (2003).
22. M. Owen, M. Bhuiyan, Q. Zhou, Z. Zhang, J. Pan, and Y. Yeo, *Appl. Phys. Lett.*, **104**, 091605 (2014).
23. L. Niinisto, J. Paivasaari, J. Niinisto, M. Putkonen, and M. Nieminen, *Phys. Status Solidi A*, **201**, 1443 (2004).
24. H. Kim, H. Lee, and W. Maeng, *Thin Solid Films*, **517**, 2563 (2009).
25. J. Dendooven, D. Deduytsche, J. Musschoot, R. Vanmeirhaeghe, and C. Detavernier, *J. Electrochem. Soc.*, **157**, G111 (2010).
26. Y. Zhang, D. Seghete, A. Abdulagatov, Z. Gibbs, A. Cavanagh, R. Yang, S. George, and Y. Lee, *Surf. Coat. Tech.*, **205**, 3334 (2011).
27. J. Lee, H. Kim, and S. Kim, *Thin Solid Films*, **577**, 143 (2015).
28. J. Van Hemmen, S. Heil, J. Klootwijk, F. Roozeboom, C. Hodson, M. van de Sanden, and W. Kessels, *J. Electrochem. Soc.*, **154**, G165 (2007).
29. K. Hubbard and D. Schlom, *J. Mater. Res.*, **11**, 2757 (1996).
30. S. Shestaeva, A. Bingel, P. Munzert, L. Ghazaryan, C. Patzig, A. Tunnermann, and A. Szeghalmi, *Appl. Opt.*, **56**, C47 (2017).
31. T. Ahmadzada, D. McKenzie, N. James, Y. Yin, and Q. Li, *Thin Solid Films*, **591**, 131 (2015).
32. R. Nakamura, T. Toda, S. Tsukui, M. Tane, M. Ishimaru, T. Suzuki, and H. Nakajima, *J. Appl. Phys.*, **116**, 033504 (2014).
33. M. Zhou, *Microelectron. Rel.*, **55** 2705 (2015).
34. C. Struller, P. Kelly, N. Copeland, V. Tobin, H. Assender, C. Holliday, and S. Read, *Thin Solid Films*, **553**, 153 (2014).
35. A. Singh, H. Klumbies, U. Schroder, L. Muller-Meskamp, M. Geidel, M. Knaut, C. Hobbach, M. Albert, K. Leo, and T. Mikolajick, *Appl. Phys. Lett.*, **103**, 233302 (2013).
36. P. Majumder, R. Katamreddy, and C. Takoudis, *Electrochem. Sol. Stat. Lett.*, **10**, H291 (2007).
37. V. Zhirnov, R. Cavin III, J. Hutchby, and G. Bourianoff, *Proc. IEEE*, **91**, 1934 (2003).
38. J. Shen, *J. Vac. Sci. Technol. B*, **17**, 2115 (1999).
39. E. Pop, *Nano. Res.*, **3**, 147 (2010).
40. L. Wang, A. R. Brown, M. Nedjalkov, C. Alexander, B. Cheng, C. Miller, and A. Asenov, *IEEE Trans. Elect. Dev.*, **62**, 2106 (2015).
41. A. A. Orouji and M. Mehrad, *Jpn. J. Appl. Phys.*, **50**, 124303 (2011).
42. M. Tripp, C. Stampfer, D. Miller, T. Helbling, C. Herrmann, C. Hierold, K. Gall, S. George, and V. Bright, *Sens. Act. A*, **130**, 419 (2006).
43. V. Mastronardi, L. Ceseracciu, F. Guido, F. Rizzi, A. Athanassiou, M. De Vittorio, and S. Petroni, *Appl. Phys. Lett.*, **106**, 162901 (2015).
44. J. A. Rogers, *MRS Bull*, **39**, 549 (2014).
45. J. P. Rojas, G. A. T. Sevilla, M. T. Ghoneim, S. B. Inayat, S. M. Ahmed, A. M. Hussain, and M. M. Hussain, *ACS Nano*, **8**, 1468 (2014).
46. N. V. Lavrik, M. J. Sepaniak, and P. G. Datskos, *Rev. Sci. Instr.*, **75**, 2229 (2004).
47. C. Guthy, R. M. Das, B. Drobot, and S. Evoy, *J. Appl. Phys.*, **108**, 014306 (2010).
48. O. Y. Loh and H. D. Espinosa, *Nat. Nanotech.*, **7**, 293 (2012).
49. C. Herrmann, F. DelRio, D. Miller, S. George, V. Bright, J. Ebel, R. Strawser, R. Cortez, and K. Leedy, *Sens. Act. A*, **135**, 262 (2007).
50. H.-Y. Chang, S. Yang, J. Lee, L. Tao, W.-S. Hwang, D. Jena, N. Lu, and D. Akinwande, *ACS Nano*, **7**, 5446 (2013).
51. G. Cantarella, C. Vogt, R. Hopf, N. Munzenrieder, P. Andrianakis, L. Petti, A. Daus, S. Knobelspies, L. Buthe, G. Troster, and G. A. Salvatore, *ACS Appl. Mater. Int.*, **9**, 28750 (2017).
52. M. Darnon, T. Chevolleau, O. Joubert, S. Maitrejean, J. C. Barbe, and J. Torres, *Appl. Phys. Lett.*, **91**, 194103 (2007).
53. G. Stan, C. V. Ciobanu, I. Levin, H. J. Yoo, A. Myers, K. Singh, C. Jezewski, B. Miner, and S. W. King, *Nano Lett*, **15**, 3845 (2015).
54. J. Wang, B. Li, Y.-P. Cao, X.-Q. Feng, and H. Gao, *Appl. Phys. Lett.*, **108**, 021903 (2016).
55. H. Jiang, Y. Sun, J. A. Rogers, and Y. Huang, *Appl. Phys. Lett.*, **90**, 133119 (2007).
56. M. Panzer, M. Shandalov, J. Rowlette, Y. Oshima, Y. Chen, P. McIntyre, and K. Goodson, *IEEE Elect. Dev. Lett.*, **30**, 1269 (2009).
57. N. Gabriel and J. Talghader, *J. Appl. Phys.*, **110**, 043526 (2011).
58. C. Gorham, J. Gaskins, G. Parsons, M. Losego, and P. Hopkins, *Appl. Phys. Lett.*, **104**, 253107 (2014).
59. Z. Luo, H. Liu, B. Spann, Y. Feng, P. Ye, Y. Chen, and X. Xu, *Nanoscale Microscale Thermophys. Engr.*, **18**, 183 (2014).
60. K. Tapily, J. Jakes, D. Stone, P. Shrestha, D. Gu, H. Baumgart, and A. Elmustafa, *J. Electrochem. Soc.*, **155**, H545 (2008).
61. B. Ilic, S. Krylov, and H. Craighead, *J. Appl. Phys.*, **108**, 044317 (2010).
62. S. Bull, *J. Vac. Sci. Technol. A*, **30**, 01A160 (2012).
63. M. Berdova, T. Ylitalo, I. Kassamakov, J. Heino, P. Torma, L. Kilpi, H. Ronkainen, J. Koskinen, E. Haeggstrom, and S. Franssila, *Acta Mater*, **66**, 370 (2014).
64. O. Ylivaara, X. Liu, L. Kilpi, J. Lyytinen, D. Schneider, M. Laitinen, J. Julin, S. Ali, S. Sintonen, M. Berdova, E. Haimi, T. Sajavaara, H. Ronkainen, H. Lipsanen, J. Koskinen, S. Hannula, and R. Puurunen, *Thin Solid Films*, **552**, 124 (2014).
65. T. Homola, V. Bursikova, T. Ivanova, P. Soucek, P. Maydannik, D. Cameron, and J. Lackner, *Surf. Coat. Tech.*, **284**, 198 (2015).
66. T. Jogiaas, R. Zabels, A. Tamm, M. Merisalu, I. Hussainova, M. Heikkila, H. Mandar, K. Kukli, M. Ritala, and M. Leskela, *Surf. Coat. Tech.*, **282**, 36 (2015).
67. J. Robertson and B. Falabretti, *J. Appl. Phys.*, **100**, 014111 (2006).
68. J. Tao, J. W. Chai, Z. Zhang, J. S. Pan, and S. J. Wang, *Appl. Phys. Lett.*, **104**, 232110 (2014).
69. A. K. Singh, R. G. Hennig, A. V. Davydov, and F. Tavazza, *Appl. Phys. Lett.*, **107**, 053106 (2015).
70. H.-Y. Chou, V. V. Afanas'ev, M. Houssa, A. Stesmans, L. Dong, and P. D. Ye, *Appl. Phys. Lett.*, **101**, 082114 (2012).
71. Q. Zhang, G. Zhou, H. G. Xing, A. C. Seabaugh, K. Xu, H. Sio, O. A. Kirillov, C. A. Richter, and N. V. Nguyen, *Appl. Phys. Lett.*, **100**, 102104 (2012).
72. G. K. Dalapati, H.-J. Oh, S. J. Lee, A. Sridhara, A. S. W. Wong, and D. Chi, *Appl. Phys. Lett.*, **92**, 042120 (2008).
73. J. Yang, B. S. Eller, C. Zhu, C. England, and R. J. Nemanich, *J. Appl. Phys.*, **112**, 053710 (2012).
74. S. Toyoda, T. Shinohara, H. Kumigashira, M. Oshima, and Y. Kato, *Appl. Phys. Lett.*, **101**, 231607 (2012).
75. T. Li, B. Wan, G. Du, B. Zhang, and Z. Zeng, *AIP Adv*, **5**, 057102 (2015).
76. S. Son, S. Yu, M. Choi, D. Kim, and C. Choi, *Appl. Phys. Lett.*, **106**, 021601 (2015).
77. S. McDonnell, B. Brennan, A. Azcatl, N. Lu, H. Dong, C. Buie, J. Kim, C. L. Hinkle, M. J. Kim, and R. M. Wallace, *ACS Nano*, **7**, 10354 (2013).
78. B. Hoex, S. B. S. Heil, E. Langereis, M. C. M. van de Sanden, and W. M. M. Kessels, *Appl. Phys. Lett.*, **89**, 042112 (2006).
79. T. M. Mayer, J. W. Elam, S. M. George, P. G. Kotula, and R. S. Goeke, *Appl. Phys. lett.*, **82**, 2883 (2003).
80. Y.-J. Chang, J. M. Gray, A. Imtiaz, D. Seghete, T. Mitch Wallis, S. M. George, P. Kabos, C. T. Rogers, and V. M. Bright, *Sens. Act. A*, **154**, 229 (2009).
81. N. D. Hoivik, J. W. Elam, R. J. Linderman, V. M. Bright, S. M. George, and Y. C. Lee, *Sens. Act. A*, **103**, 100 (2003).
82. L. A. Ragnarsson, N. A. Bojarczuk, M. Copel, E. P. Gusev, J. Karasinski, and S. Guha, *J. Appl. Phys.*, **93**, 3912 (2003).
83. Y. J. Lee, *J. Cryst. Growth*, **266**, 568 (2004).
84. D. Eom, S. Y. No, C. S. Hwang, and H. J. Kim, *J. Electrochem. Soc.*, **153**, C229 (2006).
85. F. Hasegawa, T. Takayashi, K. Kubo, and Y. Nannichi, *Jpn. J. Appl. Phys.*, **26**, 1555 (1987).
86. X.-Y. Liu, S.-X. Zhao, L.-Q. Zhang, H.-F. Huang, J.-S. Shi, C.-M. Zhang, H.-L. Lu, P.-F. Wang, and D. W. Zhang, *Nanoscale Res*, **10**, 109 (2015).
87. D. Liufu and K. C. Kao, *J. Vac. Sci. Technol. A*, **16**, 2360 (1999).
88. M.-A. Dubois and P. Muralt, *Appl. Phys. Lett.*, **74**, 3032 (1999).
89. S. Dhungana, T. D. Nguyen, B. J. Nordell, A. N. Caruso, M. M. Paquette, G. Chollon, W. A. Lanford, K. Scharfenberger, D. Jacob, and S. W. King, *J. Vac. Sci. Technol. A*, **35**, 021510 (2017).
90. A. Perros, M. Bosund, T. Sajavaara, M. Laitinen, L. Sainiemi, T. Huhtio, and H. Lipsanen, *J. Vac. Sci. Technol. A*, **30**, 011504 (2012).
91. K. Kolari, *Microelectron. Eng.*, **85**, 985 (2008).
92. W.-E. Fu, C.-W. Chang, Y.-Q. Chang, C.-K. Yao, and J.-D. Liao, *Appl. Surf. Sci.*, **258**, 8974 (2012).
93. W.-E. Fu, B.-C. He, and Y.-Q. Chang, *Thin Solid Films*, **544**, 212 (2013).
94. S. Jena, R. B. Tokas, J. S. Misal, K. D. Rao, D. V. Udupa, S. Thakur, and N. K. Sahoo, *Thin Solid Films*, **592**, 135 (2015).
95. A. Q. Wang, J. Wang, M. J. D'lallo, J. E. Platten, J. C. Crifasi, and B. P. Roy, *Thin Solid Films*, **592**, 232 (2015).
96. Y.-L. Cheng, K.-C. Kao, G.-S. Chen, J.-S. Fang, C.-R. Sun, and W.-H. Lee, *Microelectron. Eng.*, **162**, 34 (2016).
97. L. Guo, X. Qin, and F. Zaera, *ACS Appl. Mater. Inter.*, **8**, 6293 (2016).
98. S. Capone, G. Leo, R. Rella, P. Siciliano, L. Vasanelli, M. Alvisi, L. Mirenghi, and A. Rizzo, *J. Vac. Sci. Technol. A*, **16**, 3564 (1998).
99. M. Godlewski, S. Gieraltowska, L. Wachnicki, R. Pietuszka, B. Witkowski, A. Slonska, Z. Gajewski, and M. Godlewski, *J. Vac. Sci. Technol. A*, **35**, 021508 (2017).
100. A. Pal, V. K. Narasimhan, S. Weeks, K. Littau, D. Pramanik, and T. Chiang, *Appl. Phys. Lett.*, **110**, 022903 (2017).
101. J. Muller, T. Boscke, U. Schroder, S. Mueller, D. Brauhaus, U. Bottger, L. Frey, and T. Mikolajick, *Nano Lett*, **12**, 4318 (2012).
102. J. Muller, P. Polakowski, S. Mueller, and T. Mikolajick, *ECS J. Solid State Sci. Technol.*, **4**, N30 (2015).
103. F. A. McGuire, Y.-C. Lin, K. Price, G. B. Rayner, S. Khandelwal, S. Salahuddin, and A. D. Franklin, *Nano Lett*, **17**, 4801 (2017).

104. T. Peltier, R. Takahashi, and M. Lippmaa, *Appl. Phys. Lett.*, **104**, 231608 (2014).
105. J. H. Yum, T. Akyol, M. Lei, D. A. Ferrer, T. W. Hudnall, M. Downer, C. W. Bielawski, G. Bersuker, J. C. Lee, and S. K. Banerjee, *Appl. Phys. Lett.*, **99**, 033502 (2011).
106. J. H. Yum, G. Bersuker, T. Akyol, D. A. Ferrer, M. Lei, K. W. Park, T. W. Hudnall, M. C. Downer, C. W. Bielawski, E. T. Yu, J. Price, J. C. Lee, and S. K. Banerjee, *IEEE Trans. Elect. Dev.*, **58**, 4384 (2011).
107. J. H. Yum, T. Akyol, M. Lei, T. Hudnall, G. Bersuker, M. Downer, C. W. Bielawski, J. C. Lee, and S. K. Banerjee, *J. Appl. Phys.*, **109**, 064101 (2011).
108. M. Lei, J. H. Yum, J. Price, T. W. Hudnall, C. W. Bielawski, S. K. Banerjee, P. S. Lysaght, G. Bersuker, and M. C. Downer, *Appl. Phys. Lett.*, **100**, 133906 (2012).
109. D. W. Johnson, J. H. Yum, T. W. Hudnall, R. M. Mushinski, C. W. Bielawski, J. C. Roberts, W.-E. Wang, S. K. Banerjee, and H. R. Harris, *J. Electron. Mater.*, **43**, 151 (2014).
110. Y. R. Ryu, T. S. Lee, J. A. Lubguban, A. B. Corman, H. W. White, J. H. Leem, M. S. Han, Y. S. Park, C. J. Youn, and W. J. Kim, *Appl. Phys. Lett.*, **88**, 052103 (2006).
111. J. M. Khoshman, P. Jakkala, D. C. Ingram, and M. E. Kordesch, *J. Non-Cryst. Sol.*, **440**, 31 (2016).
112. H. Liang, Z. Mei, D. Ye, J. Li, W.-C. Hong, Q. Zhang, Y. Liu, L. Gu, R. Yu, Y. Lu, and X. Du, *Phys. Stat. Sol. RRL*, **11**, 1600443 (2017).
113. W. A. Pliskin, *J. Vac. Sci. Technol.*, **14**, 1064 (1977).
114. K. Maex, M. R. Baklanov, D. Shamiryan, F. Iacopi, S. H. Brongersma, and Z. S. Yanovitskaya, *J. Appl. Phys.*, **93**, 8793 (2003).
115. G. Lucovsky and J. C. Phillips, *J. Non. Cryst. Sol.*, **227**, 1221 (1998).
116. L. Wang, H. Qin, W. Zhang, L. Zhang, and D. Yan, *Thin Solid Films*, **545**, 514 (2013).
117. K. T. Butler, M. P. W. E. Lamers, A. W. Weeber, and J. H. Harding, *J. Appl. Phys.*, **110**, 124905 (2011).
118. D. Li, T. Kunz, N. Wolf, J. P. Liebig, S. Wittmann, T. Ahmad, M. T. Hessmann, R. Auer, M. Goken, and C. J. Brabec, *Thin Solid Films*, **583**, 25 (2015).
119. S. W. King, *ECS J. Solid State Sci. Technol.*, **4**, N3029 (2015).
120. A. S. Lee, N. Rajagopalan, M. Le, B. H. Kim, and H. M'Saad, *J. Electrochem. Soc.*, **151**, F7 (2004).
121. A. Noori, S. Hung, T. E. Sato, M. Bevan, K. Choi, B. McDougall, J. Swenberg, and M. Mahajani, *Nanochip Technology Journal*, **9** (2), 19 (2011).
122. J. Yum, T. Akyol, M. Lei, D. Ferrer, T. Hudnall, M. Downer, C. Bielawski, G. Bersuker, J. Lee, and S. Banerjee, *J. Cryst. Growth*, **334**, 126 (2011).
123. J. Yum, T. Akyol, M. Lei, D. Ferrer, T. Hudnall, M. Downer, C. Bielawski, G. Bersuker, J. Lee, and S. Banerjee, *Thin Solid Films*, **520**, 3091 (2012).
124. D. Koh, J. Yum, S. Banerjee, T. Hudnall, C. Bielawski, W. Lanford, B. French, P. Henry, H. Li, M. Kuhn, and S. King, *J. Vac. Sci. Technol. B*, **32**, 03D117 (2014).
125. S. King, M. French, M. Jaehnig, M. Kuhn, B. Boyanov, and B. French, *J. Vac. Sci. Technol. B*, **29**, 051207 (2011).
126. B. French and S. King, *J. Mater. Res.*, **28**, 2771 (2013).
127. W. Keuning, P. Van de Weijer, H. Lifka, W. M. M. Kessels, and M. Creatore, *J. Vac. Sci. Technol. A*, **30**, 01A131 (2012).
128. R. Saha and W. D. Nix, *Acta Mater*, **50**, 23 (2002).
129. E. T. Swartz and R. O. Pohl, *Rev. Mod. Phys.*, **61**, 605 (1989).
130. W. Lanford, M. Parenti, B. Nordell, M. Paquette, A. Caruso, M. Mantymaki, J. Hamalainen, M. Ritala, K. Klepper, V. Miikkulainen, O. Nilsen, W. Tennhaeff, N. Dudney, D. Koh, S. Banerjee, E. Mays, J. Bielefeld, and S. King, *Nucl. Instr. Meth. B*, **371**, 211 (2016).
131. S. King, J. Bielefeld, M. French, and W. Lanford, *J. Non-Cryst. Sol.*, **357**, 3602 (2011).
132. S. King, M. French, J. Bielefeld, and W. Lanford, *J. Non-Cryst. Sol.*, **357**, 2970 (2011).
133. S. King and M. Milosevic, *J. Appl. Phys.*, **111**, 73109 (2012).
134. M. Milosevic and S. King, *J. Appl. Phys.*, **112**, 93514 (2012).
135. S. King, M. French, M. Jaehnig, M. Kuhn, and G. Xu, *ECS J. Solid State Sci. Technol.*, **1**, P250 (2012).
136. S. King, J. Bielefeld, G. Xu, W. Lanford, Y. Matsuda, R. Dauskardt, N. Kim, D. Hondongwa, L. Olasov, B. Daly, G. Stan, M. Liu, D. Dutta, and D. Gidley, *J. Non-Cryst. Sol.*, **379**, 67 (2013).
137. S. King, R. Chu, G. Xu, and J. Huening, *Thin Solid Films*, **518**, 4898 (2010).
138. Y. Lin, Y. Xiang, T. Tsui, and J. Vlassak, *Acta Mater*, **56**, 4932 (2008).
139. P. Flinn, D. Gardner, and W. Nix, *IEEE Trans. Elect. Dev.*, **34**, 689 (1987).
140. S. King, L. Ross, H. Li, G. Xu, J. Bielefeld, R. Atkins, P. Henneghan, K. Davis, D. Johnson, and W. Lanford, *J. Non-Cryst. Sol.*, **389**, 78 (2014).
141. C. Janssen, M. Abdalla, F. van Keulen, B. Pujada, and B. van Venrooy, *Thin Solid Films*, **517**, 1858 (2009).
142. S. Davis and G. Guiterrez, *J. Phys.: Condens. Matter*, **23**, 495401 (2011).
143. P. Vashishta, R. Kalia, A. Nakano, and J. Rino, *J. Appl. Phys.*, **109**, 033514 (2011).
144. J. Wang, H. Li, and R. Stevens, *J. Mater. Sci.*, **27**, 5397 (1992).
145. T. Phung, D. Johnson, and G. Antonelli, *J. Appl. Phys.*, **100**, 64317 (2006).
146. J. Braun, S. King, J. Gaskins, M. Sato, T. Fujiseki, H. Fujiwara, and P. Hopkins, *Appl. Phys. Lett.*, **109**, 191905 (2016).
147. P. Hopkins, J. Serrano, L. Phinney, S. Kearney, T. Grasser, and C. Harris, *J. Heat Transfer*, **132**, 081302 (2010).
148. P. Hopkins, B. Kaehr, L. Phinney, D. Dunphy, C. Brinker, F. Garcia, T. Koehler, and A. Grillet, *J. Heat Transfer*, **133**, 061601 (2011).
149. Y. Touloukian and E. Buyco, *Thermophysical Properties of Matter-Specific Heat: Metallic Elements and Alloys*, (IFI/Plenum, New York, 1970), Vol. **4**.
150. Y. Touloukian and E. Buyco, *Thermophysical Properties of Matter-Specific Heat: Nonmetallic Solids*, (IFI/Plenum, New York, 1970), Vol. **5**.
151. S. King, D. Jacob, D. Vanleuven, B. Colvin, J. Kelly, M. French, J. Bielefeld, D. Dutta, M. Liu, and D. Gidley, *ECS J. Solid State Sci. Technol.*, **1**, N115 (2012).
152. H. Profijt, S. Potts, M. van de Sanden, and W. Kessels, *J. Vac. Sci. Technol. A*, **29**, 050801 (2011).
153. M. Hur, J. Lee, W. Kang, J. Lee, Y. Song, S. Kim, and I Kim, *Thin Solid Films*, **619**, 342 (2016).
154. C. Morterra and G. Magnacca, *Catal. Today*, **27**, 497 (1996).
155. G. Priya, P. Padmaja, K. Warrier, A. Damodaran, and G. Aruldhas, *J. Mat. Sci. Lett.*, **16**, 1584 (1997).
156. E. Langereis, M. Creatore, S. Heil, M. van de Sanden, and W. Kessels, *Appl. Phys. Lett.*, **89**, 081915 (2006).
157. M. Bosund, T. Sajavaara, M. Laitinen, T. Huhtio, M. Putkonen, V. Airaksinen, and H. Lipsanen, *Appl. Surf. Sci.*, **257**, 7827 (2011).
158. M. Broas, P. Sippola, T. Sajavaara, V. Vuorinen, A. Perros, H. Lipsanen, and M. Paulasto-Krockel, *J. Vac. Sci. Technol. A*, **34**, 041506 (2016).
159. Y. Kim, J. Provine, S. Walch, J. Park, W. Phuthong, A. Dadlani, H. Kim, P. Schindler, K. Kim, and F. Prinz, *ACS Appl. Mater. Inter.*, **8**, 17599 (2016).
160. P. Motamedi and K. Cadien, *Appl. Surf. Sci.*, **315**, 104 (2014).
161. P. Motamedi and K. Cadien, *J. Cryst. Growth*, **421**, 45 (2015).
162. T. Hirvikorpi, R. Laine, M. Vaha-Nissi, V. Kilpi, E. Salo, W. Li, S. Lindfors, J. Vartiainen, E. Kentta, J. Nikkola, A. Harlin, and J. Kostamo, *Thin Solid Films*, **550**, 164 (2014).
163. D. Goldstein, J. McCormick, and S. George, *J. Phys. Chem. C*, **112**, 19530 (2008).
164. R. Katamreddy, R. Inman, G. Jursich, A. Soulet, and C. Takoudis, *J. Electrochem. Soc.*, **153**, C701 (2006).
165. Y. Catherine and A. Talebian, *J. Electron. Mater.*, **17**, 127 (1988).
166. C. Cibert, H. Hidalgo, C. Champeaux, P. Tristant, C. Tixier, J. Desmaison, and A. Catherinot, *Thin Solid Films*, **516**, 1290 (2008).
167. R. Patel, D. Chiavetta, and C. Wolden, *J. Vac. Sci. Technol. A*, **29**, 61508 (2011).
168. M. Alevli, C. Ozgit, I. Donmez, and N. Biyikli, *J. Vac. Sci. Technol. A*, **30**, 021506 (2012).
169. G. Sanchez, P. Tristant, C. Dublanche-Tixier, F. Tetard, and A. Bologna Alles, *Surf. Coat. Tech.*, **256**, 3 (2014).
170. H. Harris, N. Biswas, H. Temkin, S. Gangopadhyay, and M. Strathman, *J. Appl. Phys.*, **90**, 5825 (2001).
171. J. Dupuie and E. Gulari, *J. Vac. Sci. Technol. A*, **10**, 18 (1992).
172. K. Chakrabarti, K. Chattopadhyay, S. Chaudhuri, and A. Pal, *Mat. Chem. Phys.*, **50**, 50 (1997).
173. C. Duquenne, M. Besland, P. Tessier, E. Gautron, Y. Scudeller, and D. Averty, *J. Phys. D: Appl. Phys.*, **45**, 015301 (2012).
174. A. Collins, E. Lightowlers, and P. Dean, *Phys. Rev.*, **158**, 833 (1967).
175. T. Kidchob, L. Malfatti, F. Serra, P. Falcaro, S. Enzo, and P. Innocenzi, *J. Sol-Gel Sci. Tech.*, **42**, 89 (2007).
176. D. Neumayer and E. Cartier, *J. Appl. Phys.*, **90**, 1801 (2001).
177. E. Loh, *Phys. Rev.*, **166**, 673 (1968).
178. T. Tague Jr. and L. Andrews, *J. Am. Chem. Soc.*, **115**, 12111 (1993).
179. C. Ozgit, I. Donmez, M. Alevli, and N. Biyikli, *Thin Solid Films*, **520**, 2750 (2012).
180. D. Hausmann and R. Gordon, *J. Crystal Growth*, **249**, 251 (2003).
181. M. Ritala, M. Leskela, L. Niinisto, T. Prohaska, G. Friedbacher, and M. Grasserbauer, *Thin Solid Films*, **250**, 72 (1994).
182. L. Zhang, H. Jiang, C. Liu, J. Dong, and P. Chow, *J. Phys. D: Appl. Phys.*, **40**, 3707 (2007).
183. S. Jakschik, U. Schroeder, T. Hecht, M. Gutsche, H. Seidl, and J. W. Bartha, *Thin Solid Films*, **425**, 216 (2003).
184. J. Yum, T. Akyol, M. Lei, T. Hudnall, G. Bersuker, M. Downer, C. Bielawski, J. Lee, and S. Banerjee, *J. Appl. Phys.*, **109**, 064101 (2011).
185. J. C. Phillips, *J. Vac. Sci. Technol. B*, **17**, 1803 (1999).
186. S. Potts, G. Dingemans, C. Lachaud, and W. Kessels, *J. Vac. Sci. Technol. A*, **30**, 021505 (2012).
187. J. Lim and Su. Yun, *Electrochem. Sol. Stat. Lett.*, **7**, F45 (2004).
188. K. Shih and D. Dove, *J. Vac. Sci. Technol. A*, **12**, 321 (1994).
189. M. Groner, J. Elam, F. Fabreguette, and S. George, *Thin Solid Films*, **413**, 186 (2002).
190. D. Triyoso, M. Ramon, R. Hegde, D. Roan, R. Garcia, J. Baker, X. Wang, P. Fejes, B. White Jr., and P. Tobin, *J. Electrochem. Soc.*, **152**, G203 (2005).
191. S. Jena, R. Tokas, J. Misal, K. Rao, D. Udupa, S. Thakur, and N. Sahoo, *Thin Solid Films*, **592**, 135 (2015).
192. T. Takagi, K. Matsubara, and H. Takaoka, *J. Appl. Phys.*, **51**, 5419 (1980).
193. S. Han and E. Aydil, *J. Appl. Phys.*, **83**, 2172 (1998).
194. K. Joshi, R. Jain, R. Pandya, B. Ahuja, and B. Sharma, *J. Chem. Phys.*, **111**, 163 (1999).
195. J. Phillips, *Rev. Mod. Phys.*, **42**, 317 (1970).
196. J. O'Dwyer, *J. Appl. Phys.*, **37**, 599 (1966).
197. E. Snow, A. Grove, B. Deal, and C. Sah, *J. Appl. Phys.*, **36**, 1664 (1965).
198. J. Simmons, *Phys. Rev.*, **155**, 657 (1967).
199. A. Kerber and E. A. Cartier, *IEEE Trans. Dev. Mater. Rel.*, **9**, 147 (2009).
200. E. Lenzlinger and E. Snow, *J. Appl. Phys.*, **40**, 278 (1969).
201. S. Sze, *J. Appl. Phys.*, **38**, 2951 (1967).
202. G. Brown, W. Robinette Jr., and H. Carlson, *J. Electrochem. Soc.*, **115**, 948 (1968).
203. A. Sinha and T. Smith, *J. Appl. Phys.*, **49**, 2756 (1978).
204. A. Lowe, M. Powell, and S. Elliot, *J. Appl. Phys.*, **59**, 1251 (1986).
205. M. Schneider, A. Bittner, A. Klein, and U. Schmid, *Microelectron. Eng.*, **140**, 47 (2015).

206. M. Gillinger, M. Schneider, A. Bittner, P. Nicolay, and U. Schmid, *J. Appl. Phys.*, **117**, 065303 (2015).
207. H. Altuntas, C. Ozgit-Akgun, I. Donmez, and N. Biyikli, *J. Appl. Phys.*, **117**, 155101 (2015).
208. M. Mutch, P. Lenahan, and S. King, *Appl. Phys. Lett.*, **109**, 062403 (2016).
209. M. Mutch, T. Pomorski, B. Bittel, C. Cochrane, P. Lenahan, X. Liu, R. Nemanich, J. Brockman, M. French, M. Kuhn, B. French, and S. King, *Microelectron. Rel.*, **63**, 201 (2016).
210. H. Chen, K. Chen, D. Drabold, and M. Kordesch, *Appl. Phys. Lett.*, **77**, 1117 (2000).
211. K. Chen and D. Drabold, *J. Appl. Phys.*, **91**, 9743 (2002).
212. J. Batey and E. Tierney, *J. Appl. Phys.*, **60**, 3136 (1986).
213. B. Ricco, M. Azbel, and M. Brodsky, *Phys. Rev. Lett.*, **51**, 1795 (1983).
214. A. Chou, K. Lai, K. Kumar, P. Chowdhury, and J. Lee, *Appl. Phys. Lett.*, **70**, 3407 (1997).
215. G. Lucovsky and J. Phillips, *J. Vac. Sci. Technol. B*, **22**, 2087 (2004).
216. T. DiStefano and D. Eastman, *Sol. Stat. Comm.*, **9**, 2259 (1971).
217. S. Toyoda, J. Okabayashi, H. Kumigashira, M. Oshima, G. Liu, Z. Liu, K. Ikeda, and K. Usuda, *Appl. Phys. Lett.*, **87**, 102901 (2005).
218. O. Blank, H. Reisinger, R. Stengl, M. Gutsche, F. Wiest, V. Capodieci, J. Schulze, and I. Eisele, *J. Appl. Phys.*, **97**, 044107 (2005).
219. M. Specht, M. Stadele, S. Jakschik, and U. Schroder, *Appl. Phys. Lett.*, **84**, 3076 (2004).
220. H. Spahr, S. Montzka, J. Reinker, F. Hirschberg, W. Kowalsky, and H. Johannes, *J. Appl. Phys.*, **114**, 183714 (2013).
221. D. Jeong and C. Hwang, *J. Appl. Phys.*, **98**, 113701 (2005).
222. P. Maleeswaran, D. Nagulapally, R. Joshi, and A. Pradhan, *J. Appl. Phys.*, **113**, 184504 (2013).
223. R. Southwick III, J. Reed, C. Buu, R. Butler, G. Bersuker, and W. Knowlton, *IEEE Dev. Mater. Rel.*, **10**, 201 (2010).
224. S. Pan, S. Ding, Y. Huang, Y. Huang, D. Zhang, L. Wang, and R. Liu, *J. Appl. Phys.*, **102**, 073706 (2007).
225. G. Jellison and F. Modine, *Appl. Phys. Lett.*, **69**, 371 (1996).
226. C. Sire, S. Blonkowski, M. Gordon, and T. Baron, *Appl. Phys. Lett.*, **91**, 242905 (2007).
227. P. Solomon, *J. Vac. Sci. Technol. A*, **14**, 1122 (1977).
228. M. Vos, S. King, and B. French, *J. Electron. Spectrosc. Relat. Phenom.*, **212**, 74 (2016).
229. C. Kim, G. Pilania, and R. Ramprasad, *Chem. Mater.*, **28**, 1304 (2016).
230. C. Kim, G. Pilania, and R. Ramprasad, *J. Phys. Chem. C*, **120**, 14575 (2016).
231. F. Hasegawa, T. Takahashi, K. Kubo, and Y. Nannichi, *Jap. J. Appl. Phys.*, **26**, 1666 (1987).
232. R. Gordon, U. Riaz, and D. Hoffman, *J. Mater. Res.*, **7**, 1679 (1992).
233. N. Alimardani, S. King, B. French, C. Tan, B. Lampert, and J. Conley, Jr., *J. Appl. Phys.*, **116**, 024508 (2014).
234. S. Miyazaki, *J. Vac. Sci. Technol. B*, **19**, 2212 (2001).
235. D. Tahir, H. Kwon, H. Shin, S. Oh, H. Kang, S. Heo, J. Chung, J. Lee, and S. Tougaard, *J. Phys. D: Appl. Phys.*, **43**, 25530 (2010).
236. M. Di, E. Bersch, and A. Diebold, *J. Vac. Sci. Technol. A*, **29**, 041001 (2011).
237. J. McPherson, J. Kim, A. Shanware, and H. Mogul, *Appl. Phys. Lett.*, **82**, 2121 (2003).
238. J. McPherson, *Microelectron. Rel.*, **52**, 1753 (2012).
239. K. Jarolimek, R. de Groot, G. de Wijs, and M. Zeman, *Phys. Rev. B*, **82**, 205201 (2010).
240. G. Lucovsky, *J. Vac. Sci. Technol. A*, **19**, 1553 (2001).
241. S. Carniglia and J. Hove, *J. Nuc. Mater.*, **4**, 165 (1961).
242. R. Fryxell and B. Chandler, *J. Amer. Ceram. Soc.*, **47**, 283 (1962).
243. N. Chechenin, J. Bottiger, and J. Krog, *Thin Solid Films*, **304**, 70 (1997).
244. W. Oliver and G. Pharr, *J. Mater. Res.*, **7**, 1564 (1992).
245. I. Yonenaga, T. Shima, and M. Sluiter, *Jpn. J. Appl. Phys.*, **41**, 4620 (2002).
246. S. Dodd, G. Saunders, M. Cankurtaran, and B. James, *J. Mat. Sci.*, **36**, 723 (2001).
247. V. Mortet, M. Nesladek, K. Haenen, A. Morel, M. D'Olieslaeger, and M. Vanecek, *Diam. Relat. Mater.*, **13**, 1120 (2004).
248. S. Jian, G. Chen, and T. Lin, *Nanoscale Res. Lett.*, **5**, 935 (2010).
249. R. Wu, B. Zhou, Q. Li, Z. Jiang, W. Wang, W. Ma, and X. Zhang, *J. Phys. D: Appl. Phys.*, **45** 125304 (2012).
250. S. Dole, O. Hunter Jr., and C. Wooge, *J. Amer. Ceram. Soc.*, **60**, 488 (1977).
251. M. Berdova, X. Liu, C. Wiemer, A. Lamperti, G. Tallarida, E. Cianci, M. Fanciulli, and S. Franssila, *J. Vac. Sci. Technol. A*, **34**, 051510 (2016).
252. D. Venkatachalam, J. Bradby, M. Saleh, S. Ruffell, and R. Elliman, *J. Appl. Phys.*, **110**, 043527 (2011).
253. J. Zizka, S. King, A. Every, and R. Sooryakumar, *J. Appl. Phys.*, **119**, 144102 (2016).
254. R. Munro, *J. Am. Ceram. Soc.*, **80**, 1919 (1997).
255. J. Barbour, J. Knapp, D. Follstaedt, T. Mayer, K. Minor, and D. Linam, *Nucl. Instr. and Meth. B*, **166**, 140 (1994).
256. J. Proost and F. Spaepen, *J. Appl. Phys.*, **91**, 204 (2002).
257. Q. Zhang, X. Xiao, Y. Cheng, and W. Verbrugge, *Appl. Phys. Lett.*, **105**, 061901 (2014).
258. J. Thurn and R. Cook, *J. Mat. Sci.*, **39**, 4799 (2004).
259. T. Hanada, Y. Bessyo, and N. Soga, *J. Non-Cryst. Sol.*, **113**, 213 (1989).
260. R. Vogelgesang, M. Grimsditch, and J. Wallace, *Appl. Phys. Lett.*, **76**, 982 (2000).
261. J. Hay, E. Sun, G. Pharr, P. Becher, and K. Alexander, *J. Amer. Ceram. Soc.*, **81**, 2661 (1998).
262. O. Yeheskel and Y. Gefen, *Mat. Sci. Engr.*, **71**, 95 (1985).
263. T. Rouxel, J. Sangleboeuf, M. Huger, C. Gault, J. Besson, and S. Testu, *Acta Mater*, **50**, 1669 (2002).
264. J. Taylor, *J. Vac. Sci. Technol. A*, **9**, 2464 (1991).
265. P. Morin, G. Raymond, D. Benoit, P. Maury, and R. Beneyton, *Appl. Surf. Sci.*, **260**, 69 (2012).
266. G. Carlotti, P. Colpani, D. Piccolo, S. Santucci, V. Senez, G. Socino, and L. Verdini, *Thin Solid Films*, **414**, 99 (2002).
267. G. Carlotti, L. Doucet, and M. Dupeux, *Thin Solid Films*, **296**, 102 (1997).
268. P. Mante, J. Robillard, and A. Devos, *Appl. Phys. Lett.*, **93**, 071909 (2008).
269. D. Miller, R. Foster, S. Jen, J. Bertrand, S. Cunningham, A. Morris, Y. Lee, S. George, and M. Dunn, *Sens. Actuators A*, **164**, 58 (2010).
270. J. Gluch, T. Robler, S. Menzel, and J. Eckert, *Microelectron. Engr.*, **8**, 561 (2011).
271. A. Bulusu, A. Singh, C. Wang, A. Dindar, C. Fuentes-Hernandez, H. Kim, D. Cullen, B. Kippelen, and S. Graham, *J. Appl. Phys.*, **118**, 085501 (2015).
272. W. Claasen, *Plasma Chem. Plasma Proc.*, **7**, 109 (1987).
273. M. Maeda and K. Ikeda, *J. Appl. Phys.*, **83**, 3865 (1998).
274. S. King, *J. Vac. Sci. Technol. A*, **29**, 041501 (2011).
275. M. Putkonen, M. Bosund, O. Ylivaara, R. Puurunen, L. Kilpi, H. Ronkainen, S. Sintonen, S. Ali, H. Lipsanen, X. Liu, E. Haimi, S. Hannula, T. Sajavaara, I. Buchanan, E. Karwacki, and M. Vaha-Nissi, *Thin Solid Films*, **558**, 93 (2014).
276. H. Profijt, M. van de Sanden, and W. Kessels, *J. Vac. Sci. Technol. A*, **31**, 01A106 (2013).
277. J. Thurn and R. Cook, *J. Appl. Phys.*, **91**, 1988 (2002).
278. M. Hughey and R. Cook, *Thin Solid Films*, **460**, 7 (2004).
279. J. Thurn, R. Cook, M. Kamarajugadda, S. Bozeman, and L. Stearns, *J. Appl. Phys.*, **95**, 967 (2004).
280. M. Hughey and R. Cook, *J. Appl. Phys.*, **97**, 114914 (2005).
281. B. Yates, R. Cooper, and A. Pojur, *J. Phys. C*, **5**, 1046 (1972).
282. M. Halvarsson, V. Langer, and S. Vuorinen, *Surf. Coat. Tech.*, **76**, 358 (1995).
283. W. Yim and R. Paff, *J. Appl. Phys.*, **45**, 1456 (1974).
284. T. Retajczyk and A. Sinha, *Thin Solid Films*, **70**, 241 (1980).
285. F. Boey and A. Tok, *J. Mater. Proc. Tech.*, **140**, 413 (2003).
286. V. Minkiewicz, J. Stasiak, R. White, R. Cornell, J. Moore, R. Eaton, J. Eldridge, and F. Lee, *Surf. Coat. Tech.*, **68**, 229 (1994).
287. A. Sinha, H. Levinstein, and T. Smith, *J. Appl. Phys.*, **49**, 2423 (1978).
288. Y. Toivola, J. Thurn, R. Cook, G. Cibuzar, and K. Roberts, *J. Appl. Phys.*, **94**, 6915 (2003).
289. F. Jansen, M. Machonkin, N. Palmieri, and D. Kuhman, *J. Appl. Phys.*, **62**, 4732 (1987).
290. I. Blech and U. Cohen, *J. Appl. Phys.*, **53**, 4202 (1982).
291. H. Iwanaga, A. Kunishige, and S. Takeuchi, *J. Mater. Sci.*, **35**, 2451 (2000).
292. R. Haggerty, P. Sarin, Z. Apostolov, P. Driemeyer, and W. Kriven, *J. Amer. Ceram. Soc.*, **97**, 2213 (2014).
293. G. Carlotti, N. Cherault, N. Casanova, C. Goldberg, and G. Socino, *Thin Solid Films*, **493**, 175 (2004).
294. J. Vlassak and W. Nix, *J. Mater. Res.*, **7**, 3242 (1996).
295. K. Goodson, M. Flik, L. Su, and D. Antoniadis, *IEEE Elect. Dev. Lett.*, **14**, 490 (1993).
296. A. Griffin Jr., F. Brotzen, and P. Loos, *J. Appl. Phys.*, **75**, 3761 (1994).
297. Y. Ju and K. Goodson, *J. Appl. Phys.*, **84**, 7130 (1999).
298. J. Kim, A. Feldman, and D. Novotny, *J. Appl. Phys.*, **86**, 3959 (1999).
299. T. Yamane, N. Nagai, S. Katayama, and M. Todoki, *J. Appl. Phys.*, **91**, 9772 (2002).
300. S. Lee and D. Cahill, *J. Appl. Phys.*, **81**, 2590 (1997).
301. M. von Arx, O. Paul, and H. Baltes, *J. Microelectromech. Sys.*, **9**, 136 (2000).
302. N. Stojanovic, J. Yun, E. Washington, J. Berg, M. Holtz, and H. Temkin, *J. Microelectromech.*, **16**, 1269 (2007).
303. T. Coquil, E. Richman, N. Hutchinson, S. Tolbert, and L. Pilon, *J. Appl. Phys.*, **106**, 34910 (2009).
304. M. Bogner, A. Hofer, G. Benstetter, H. Gruber, and R. Fu, *Thin Solid Films*, **591**, 267 (2015).
305. W. Li and N. Mingo, *J. Appl. Phys.*, **114**, 183505 (2013).
306. G. Slack, *J. Appl. Phys.*, **42**, 4713 (1971).
307. G. Akishin, S. Turnaev, V. Vaispapir, M. Gorbunova, Y. Makurin, V. Kiiko, and A. Ivanovskii, *Ref. Ind. Ceram.*, **50**, 465 (2009).
308. G. Slack, R. Tanzilli, R. Pohl, and J. Vandersande, *J. Phys. Chem. Sol.*, **48**, 641 (1987).
309. A. Jacquot, B. Lenoir, A. Dauscher, P. Verardi, F. Craciun, M. Stolzer, M. Gartner, and M. Dinescu, *Appl. Surf. Sci.*, **186**, 507 (2002).
310. Y. Zhao, C. Zhu, S. Wang, J. Tian, D. Yang, C. Chen, H. Cheng, and P. Hing, *J. Appl. Phys.*, **96**, 4563 (2004).
311. B. Belkerk, A. Soussou, M. Carette, M. Djouadi, and Y. Scudeller, *Appl. Phys. Lett.*, **101**, 151908 (2012).
312. S. Choi, D. Kim, S. Choa, S. Lee, and J. Kim, *Int. J. Thermophys.*, **27**, 896 (2006).
313. Y. Bian, M. Liu, G. Ke, Y. Chen, J. DiBattista, E. Chan, and Y. Yang, *Surf. Coat. Tech.*, **267**, 65 (2015).
314. T. Lee, M. Burzo, P. Kumarov, P. Raad, and M. Kim, *Electrochem. Sol. Stat. Lett.*, **14**, H184 (2011).
315. J. Braun, C. Baker, A. Giri, M. Elahi, K. Artyushkova, T. Beechem, P. Norris, Z. Leseman, J. Gaskins, and P. Hopkins, *Phys. Rev. B*, **93**, 140201 (2016).
316. G. Slack, L. Schowalter, D. Morelli, and J. Freitas, Jr., *J. Crystal Growth*, **246**, 287 (2002).
317. D. Cahill, S. Lee, and T. Selinder, *J. Appl. Phys.*, **83**, 5783 (1998).
318. A. Hofmeister, *Phys. Chem. Minerals*, **41**, 361 (2014).
319. Y. Yoon, R. Car, D. Srolovitz, and S. Scandolo, *Phys. Rev. B*, **70**, 012302 (2004).

320. A. Tiwari, K. Boussois, B. Nait-Ali, D. Smith, and P. Blanchart, *AIP Adv*, **3**, 112129 (2013).
321. I. Stark, M. Stordeur, and F. Syrowatka, *Thin Solid Films*, **226**, 185 (1993).
322. M Winter and D. Clarke, *Acta Mater*, **54**, 5051 (2006).
323. C. Ramana, M. Noor-A-Alam, J. Gengler, and J. Jones, *ACS Appl. Mater. Inter.*, **4**, 200 (2012).
324. S. Lee, D. Cahill, and T. Allen, *Phys. Rev. B*, **52**, 253 (1995).
325. M. Hinz, O. Marti, B. Gotsmann, M. Lantz, and U. Durig, *Appl. Phys. Lett.*, **92**, 043122 (2008).
326. M. Grilli, D. Ristau, M. Dieckmann, and U. Willamowski, *Appl. Phys. A*, **71**, 71 (2000).
327. J. Lambropoulos, M. Jolly, C. Amsden, S. Gilman, M. Sinicropi, D. Diakomihalis, and S. Jacobs, *J. Appl. Phys.*, **66**, 4230 (1989).